JOURNAL OF SPACECRAFT AND ROCKETS
Vol. 47, No. 5, September–October 2010

Observations of the Stardust Sample Return Capsule Entry with a Slitless Echelle Spectrograph

Peter Jenniskens*
SETI Institute, Mountain View, California 94043

DOI: 10.2514/1.37518

Spectroscopic observations of the 2006 Stardust Sample Return Capsule entry are presented, obtained by means of a slitless miniature echelle spectrograph onboard NASA's DC-8 airborne laboratory. The data cover the wavelength range from 336 to 880 nm, at 0.14–0.9 nm resolution, and were obtained during the time interval when radiative heating was most important. The data contain a broadband continuum, presumably from the hot heat-shield surface, shock-layer air plasma emissions of N, O, and N_2^+, and atomic hydrogen and CN molecular band emission from the ablating heat-shield material, a form of phenol-impregnated carbon ablator. Early in flight, there were also atomic line emissions of Zn, K, Ca^+, and Na, presumably from a white Z-93P paint applied to the top of the phenol-impregnated carbon ablator. At each moment along the trajectory, the whole spectrum was recorded simultaneously, but broken into smaller segments. Key issues addressed in the data reduction and calibration are described. The interpretation of these data was given elsewhere.

Nomenclature

A	=	surface area
c	=	speed of light
D	=	diameter
d	=	distance to the source
E	=	irradiance (flux density)
f	=	function
h	=	Planck constant
j	=	horizontal pixel position
k	=	Boltzmann constant
L	=	radiance
m	=	echelle order
r	=	radius of lens
T	=	temperature
X	=	$m(1-\lambda_c)/\lambda$
α	=	echelle blaze function parameter
β	=	angle from boresight
δ	=	blaze angle
Θ	=	power
θ	=	cone acceptance
θ_C	=	camera-collimator angle
κ	=	first-order blaze wavelength
Λ	=	groove distance
λ	=	wavelength
λ_c	=	blaze wavelength
ϕ	=	fraction
Ω	=	solid angle

I. Introduction

AT A speed of 12.8 km/s, the 15 January 2006 reentry of the Sample Return Capsule of NASA's Stardust mission was the fastest-ever-attempted reentry of a spacecraft [1]. During entry, the canister containing the captured dust particles of comet 81P/Wild 2 was protected by a thermal protection system that featured an ablative heat shield made of a new material called phenol-impregnated carbon ablator (PICA). PICA was being considered as a candidate thermal protection material for the new Crew Exploration Vehicle, which made the return of Stardust the first system field test of an important thermal protection material.

During collection of the comet dust particles, Stardust had nearly matched the orbit of comet 81P/Wild 2, which put the return trajectory of the capsule on an orbit similar to that of comets, asteroids, and meteoroids. This made the return of Stardust an artificial meteoroid, with well-known entry conditions and ballistic coefficient.

With no onboard sensors to study the physical conditions during entry, an airborne observing campaign was organized to study the capsule's surface temperature, rate of ablation, and emitted shock radiation by remote sensing [1]. Several instrument principal investigator teams fielded a range of spectrometers and imagers that were both complementary and redundant in sensitivity and spectroscopic capabilities. NASA's DC-8 airborne laboratory carried these sensors to an altitude of 11.9 km, above clouds and water vapor, and to a location near the end of the grazing entry trajectory for a frontal view of the approaching capsule over much of its entry path.

For the purpose of measuring spectra at high resolution, a commercial miniature echelle spectrograph was developed into a dedicated instrument that made optical spectroscopy possible at high spectral resolution. This paper describes this instrument, the echelle-based spectrograph for the crisp and high efficient detection of low light emission (called ECHELLE), the observing procedures, and the calibration of the data.

II. Instrument

The ECHELLE consisted of a 105 mm, f4.5 UV Nikkor lens (A in Fig. 1) [2], a Catalina Scientific SE 200 echelle spectrograph (B in Fig. 1) [3], and a QImaging intensified charge-coupled-device (CCD) camera (C in Fig. 1) [4]. Factory-provided specifications for instrument components are listed in Table 1. The optical layout (Ebert configuration) consisted of an entrance aperture (A in Fig. 1), a dispersion module that contained the grating and order-sorting prism (B in Fig. 1), and a collimator made of internal mirrors (C in Fig. 1). Manual tracking was done by using a coaligned low-light-level video camera (D in Fig. 1), the output of which was viewed by means of a video headset display with crosshairs.

The SE 200 system had a focal length of 200 mm, making this an f10 instrument. Focusing the lens achieved coarse focus. Two flat

Presented as Paper 2008-1210 at the 46th AIAA Aerospace Sciences Meeting and Exhibit, Reno, NV, 7–10 January 2008; received 12 March 2008; revision received 1 July 2010; accepted for publication 2 July 2010.

*Research Scientist, Principal Investigator of the Stardust Sample Return Capsule entry observing campaign, Carl Sagan Center, 515 North Whisman Road. Member AIAA.

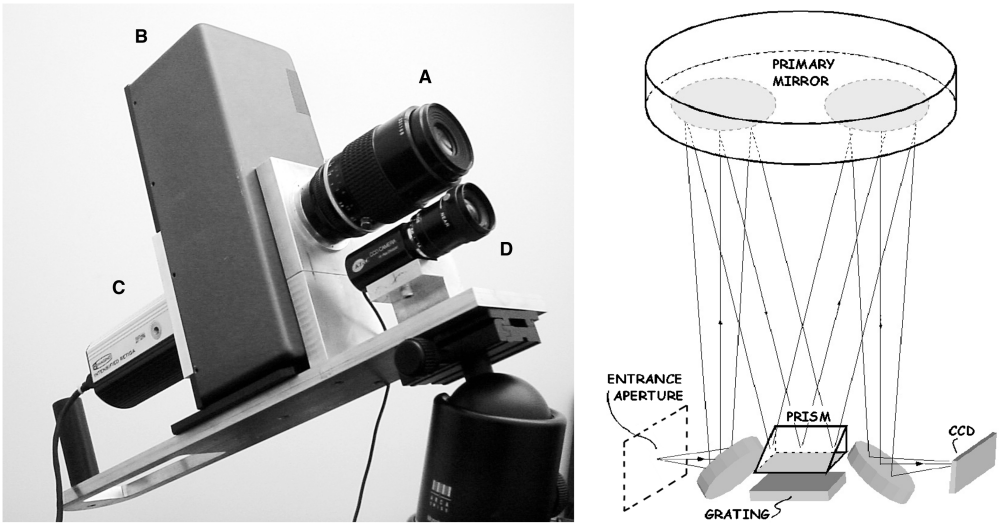

Fig. 1 Slitless miniature echelle spectrograph ECHELLE. Right: instrument layout courtesy of Catalina Scientific [5]. Letter designations are explained in the text.

mirrors and a concave mirror refocused the image plane at the aperture back on the CCD, after passing through the dispersion module as a beam of parallel rays (Fig. 1). A focusing screw adjusted the focus by moving the primary mirror to focus the image on the CCD (in our case, the photocathode of the intensifier tube).

The standard 25 μm entrance aperture was removed from the system. This left a large opening of 20.0 mm, or an image plane of a 1.64 deg field of view. In its place was put an aluminum support for the Nikon lens (diaphragm set at $f5.6$). The six-element quartz/fluorspar glass lens was designed for operation in a broad wavelength range from 220 to 880 nm (greater than 70% transmission) [2]. There was virtually no variation in the focus position (aberration or spatial distortion) between visible and UV rays, but temperature could change the focus due to the use of fluorite (CaF_2) in some of the elements. Special antireflection coating was used to reduce the reflection of UV rays.

The SE 200 standard dispersion module was chosen as the dispersive element, because it provided the highest-order separation, compared to other available modules (SE 200 high-order and SE 200 UV). The system provided a linear wavelength scale over each order, but the scale changed with order. The resolving power was, on average, $\lambda/\Delta\lambda = 1700$ when used with an intensified CCD camera [5]. Scattered light was effectively suppressed.

The SE 200 standard dispersion module required a CCD sensor that was at least 12×12 mm in size to capture the complete spectrum. Using too small a CCD would cause some gaps to appear in the spectral curves. To good effect, the 12-bit QIMaging Intensified Retiga [4] camera was used with an 8.97×6.71 mm array. This caused the edges of the echelle orders to be lost, but did not result in loss of wavelength coverage, as individual orders continued to overlap. The CCD was read at a rate of 10 frames per second for full resolution (1×1 binning during flight) at 12-bit digitization (4096 gray levels). The gamma was set to 1.0 during flight. The gamma setting controls contrast in the grayscale reproduced from the CCD readout. CCDs have a linear response as long as gamma is set to 1.0. The range of CCD gain control varied from 0.7 to 30 times and was set at 1.0 during fight.

The intensified CCD (ICCD) camera used an 18 mm Extended Blue Gen III image intensifier with GaAs photocathode and high-speed-intensifier gate control for nanosecond exposures (set at

Table 1 Factory-provided specifications of instrument components

Lens	Nikon 105 mm f4.5 UVNikkor
Optical elements	six-element quartz/fluorspar glass
Depth of field	59.5 m to infinity (set at infinity)
Spectrograph	Catalina Scientific, SE 200 Echellette
Dimensions	5 in. (width) by 6 in. (depth) by 12.5 in. (height)
Weight	9 lb (without intensifier and lens)
Dispersive module	SE 200 standard (serial number 035)
Grating dispersion	$1/\Lambda = 60$ grooves/mm
Blaze wavelength	$\kappa = 6700$ nm (first order)
Blaze offset	65 nm
Reflection grating	Aluminized epoxy
Prism material	Fused silica
Apex offset	0.2°
Mirrors	Aluminized BK7, bare aluminum
Clear aperture	>90% of diameter
Detector	QImaging Intensified Retiga CCD
Weight	800 g
Sensor	2/3 in. ICX285 progressive scan interline CCD monochrome sensor
Pixels	1392×1040
Pixel size	6.45×6.45 μm
CCD gain	0.7–30 (set at 1.0)
Intensifier luminous gain	IG = 0–80, 000 (set at 8000)
Intensifier	18 mm Extended Blue Gen III

Fig. 2 ECHELLE being mounted at the aircraft window by camera operator Mike Koop (bottom) and the author. Photo: NASA.

Table 2 Stardust SRC trajectory calculated after the final thrust maneuver correction (TMC-19)

UTC time 15 Jan. 2006	Since entry interface, s	Geodetic latitude, deg	Longitude, deg	Geodetic altitude, km	Elevation, deg	Range, km	Viewing angle, deg	Speed, km/s
9:57:15.0	32.72	41.2323	240.7917	82.701	7.412	434.6	10.4	12.765
9:57:16.0	33.72	41.2131	240.9349	81.367	7.558	422.4	10.7	12.750
9:57:17.0	34.72	41.1937	241.0778	80.090	7.711	410.3	10.9	12.732
9:57:18.0	35.72	41.1742	241.2205	78.810	7.872	398.2	11.2	12.709
9:57:19.0	36.72	41.1545	241.3629	77.547	8.042	386.1	11.5	12.681
9:57:20.0	37.72	41.1346	241.5049	76.303	8.220	374.1	11.8	12.649
9:57:21.0	38.72	41.1146	241.6465	75.077	8.409	362.1	12.2	12.610
9:57:22.0	39.72	41.0945	241.7876	73.870	8.608	350.1	12.5	12.564
9:57:23.0	40.72	41.0743	241.9282	72.682	8.819	338.2	12.9	12.509
9:57:24.0	41.72	41.0540	242.0680	71.514	9.042	326.4	13.3	12.445
9:57:25.0	42.72	41.0336	242.2071	70.367	9.279	314.7	13.7	12.369
9:57:26.0	43.72	41.0132	242.3453	69.241	9.530	303.1	14.2	12.274

0.100018 s during flight), and an intensifier luminous gain of up to intensifier gain (IG) = 80, 000 (which was set at 8000 during flight). The intensifier was fiber-optically coupled to the CCD. The capture software used was Q Capture Software for Microsoft Windows. Note that the IG setting was not stored in the image header.

In this configuration, the resolving power was measured to be $\lambda/\Delta\lambda = 2600$ at 370 nm and $\lambda/\Delta\lambda = 980$ at 880 nm (advertised as 1700). The spectra covered the 336–880 nm spectral range at a full width at half-maximum (FWHM) spectral resolution, increasing from FWHM = 0.14 nm at 370 nm to FWHM = 0.9 nm at 880 nm.

The spectrograph was mounted on a sturdy aluminum plate together with a small coaligned low-light-level KT&C CCD camera (Hi-Res ExVision) for pointing (Fig. 1). This camera used a Sony Ex-View CCD sensor and put out an National Television System Committee signal that was viewed by means of an I-Glasses video headset display with crosshairs.

The slitless miniature echelle spectrograph was operated on a window ball-mount swivel. The equipment was stored before takeoff and landing and mounted on the platform after takeoff. Foam protected the aircraft window during installation. Setup in flight took only a few minutes (Fig. 2).

The instrument was operated from behind a Pyrex window (serial number 85) on port 1010 on the left side of the DC-8 aircraft [6]. This is a flat window mounted at an 8 deg angle looking upward. During descent of the capsule, the spectrograph was pointed at the capsule, which changed the viewing geometry with respect to the window, but only from 15 deg aft (for first spectrum) to 10 deg aft (final spectrum).

Time [Coordinated Universal Time (UTC) 15 January 2006] was written in the image header (hh:mm:ss.sss) at the moment of writing to a buffer, before a series of frames were saved to disc. This time was synchronized to the onboard IRIG-B time code by using an Adrienne Electronics Corporation time code reader. Time from IRIG-B was Global Positioning System (GPS)-controlled, provided in the aircraft, and recorded at ± 0.001 s precision. Reduced data give the time at the center of the integration interval.

III. Results

The Stardust Sample Return Capsule (SRC) entered much as predicted, following the trajectory listed in Table 2. A total of 100 raw spectral frames were recorded (Fig. 3): files called Echelle001 through Echelle100. The first frame was written at 09:57:16.077 UTC; the last frame at 09:57:25.983 UTC. This covered the period of time when the SRC descended from 82 km altitude to 69 km altitude, while the aircraft flew level at an altitude of 11.887 km (Table 3). The SRC was at a distance of 435 − 303 km from the aircraft, appearing at 10.4–14.2° elevation, which was about 13–17° above the cloud deck.

The observations covered most of early period of entry, when a paint layer ablated, when the surface temperature increased ahead of peak heating (which occurred at 09:57:33 UTC), and when the air plasma emissions contributed most significantly to radiative heating. The capsule moved at considerable speed relative to the atmosphere at that time, decelerating from 12.8 to 12.3 km/s (Table 2).

A second set of frames written to disk immediately following the first series did not contain a signal from the SRC itself (Echelle101 to Echelle200). The images contained shot noise, but no SRC signal. This means that the intensifier and the CCD camera operated successfully, but the shutter of the camera did not open. These files were used as dark for evaluating the offset and other background signals. No additional dark frames were taken.

The spectra were perfectly exposed, due to preflight radiation prediction models [1]. The spectra showed no saturation, even in the bright emission lines, and the continuum emission (an underlying

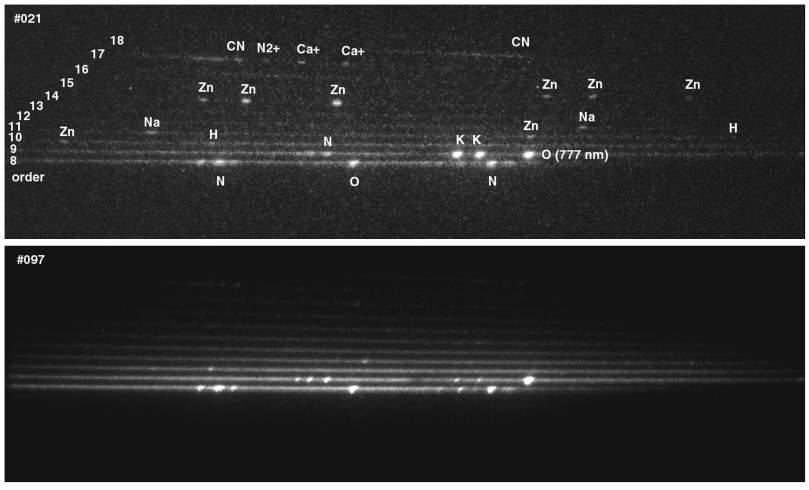

Fig. 3 Examples of raw Stardust SRC emission spectra, Echelle021 (top) and 097. The echelle orders are identified, as are the main emission features.

Table 3 Aircraft location during the observations (provided by aircraft GPS)

Time, UTC	Lat, deg	Long., deg	Alt, km
9:57:16.000	+39.90090 N	245.50742 E	11.887
9:57:18.000	+39.90403	245.51048	11.887
9:57:20.000	+39.90717	245.51358	11.887
9:57:22.000	+39.91030	245.51666	11.887
9:57:24.000	+39.91341	245.51976	11.887
9:57:26.000	+39.91653	245.52286	11.887

component to emission lines and bands) was observed until into the near-UV wavelength range (Fig. 3).

The measured pixel intensity of each order was extracted, corrected for instrumental response, and then all orders were combined into one-dimensional spectra that plot the spectral flux density E_λ, in units of (10^{-12}) W/m^2/nm, against the vacuum wavelength, as would have been observed just outside of the aircraft window after correction for extinction in the line of sight from capsule to aircraft. These emission lines are identified in Table 4, and molecular bands are identified in Table 5. The fully reduced data set, as released on 11 March 2008, is summarized in Fig. 4. The wavelength scale is reliable, with an accuracy of about $\Delta\lambda = 0.11$ nm at 800 nm to $\Delta\lambda = 0.30$ nm at 400 nm. The absolute accuracy of the flux density scale is less than 20% better in the intermediate orders.

What follows is a discussion of the data reduction, instrument definition, and environmental corrections that were applied to the data. The most difficult task was the determination of the instrument's response, mainly because of issues that affected the instrument's responsivity calibrations, but that did not directly affect the Stardust observations. Confusion was created by the use of Ocean Optics calibration lamps for measuring the instrumental response of our slitless instrument, which were designed for fiber-fed spectrometer calibrations instead (Appendix A). Postflight calibrations based on an Eppley calibration lamp revealed how the Ocean Optics calibration lamps performed differently when no fiber is used. The lamp calibration issues brought to light a number of aspects of the instrument's performance under different viewing conditions (near-field and far-field sources), instrument settings (intensifier gain), and observing conditions (stray light and temperature).

IV. Data Reduction

A. Extraction of the Spectra

A vertical cross section of the recorded continuum spectra (Fig. 5) shows that due to strong wings in the point-spread function (PSF) of the camera, the lower orders contributed significantly to emission at the position of the higher orders. The orders are about 16 pixels apart in the lower orders ($m = 8, 9$). And even though the separation increased for higher orders, the full width at half-maximum increased as well. Two possible approaches to disentangle the orders were investigated: 1) a three-dimensional deconvolution using a fast Fourier transform (FFT) algorithm (Fig. 5, left) and 2) a two-dimensional separation by fitting each order with a 2-D Lorentzian-shaped PSF (Fig. 5, right). The second method was found to perform best and was used to extract the orders.

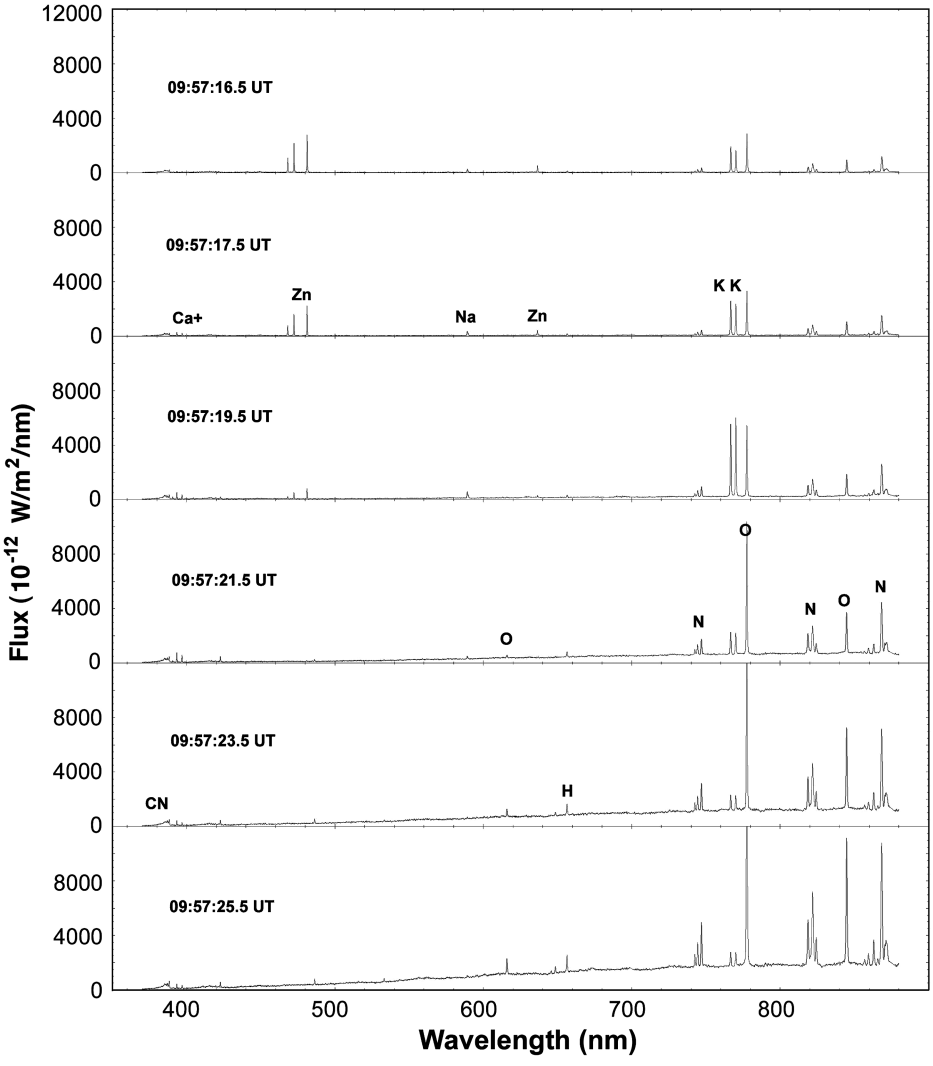

Fig. 4 Stardust SRC entry spectra. Sum of all spectra collected during 1 s intervals.

Table 4 Emission lines found in the spectra (vacuum wavelengths and energy of the upper level)

Element	λ, nm (vac)	E^{up}, eV	Order	Element	λ, nm (vac)	E^{up}, eV	Order
NI	389.3308	13.876	17 + 18	+OI	615.9853	12.755	11
Unid.	390.70	——	17	+OI	615.9876	12.755	11
CaII	393.4777	3.151	17	+OI	615.9891	12.755	11
AlI	394.5122	3.143	17	NI?	628.7616 (0.95?)	13.973	11
AlI	396.2641	3.143	17	ZnI	636.4097	7.744	10 + 11
CaII	396.9592	3.124	17	NI	644.2718	13.689	10 + 11
HI	410.2892	13.222	16 + 17	+NI	644.3491	13.689	10 + 11
+NI	410.1100	13.704	16 + 17	OI	645.5386	12.662	10 + 11
NI	411.1109	13.707	16 + 17	+OI	645.6228	12.662	10 + 11
NI	415.2652	13.322	16 + 17	+OI	645.7761	12.662	10 + 11
NI	421.5987	13.272	16	NI	648.449	13.677	10 + 11
+NI	421.7281	13.267	16	+NI	648.660	13.670	10 + 11
NI	422.3293	13.267	16	HI	656.4610	12.088	10 + 11
+NI	422.4320	13.272	16	Unid.	658.72	——	10 + 11
+NI	422.6069	13.264	16	NI	664.6797	13.630	10
+CaI?	422.7918	2.933	16	NI	672.4466	13.689	10
NI	423.1655	13.266	16	+OI	672.8140	10.990	10
NI	425.4592	13.251	16	+OI	672.8396	10.990	10
+NI	425.5930	13.244	16	OI[a]	700.4161	12.760	9 + 10
NI[b]	426.2482	13.240	16	NI	742.5686	11.996	9
HI	434.1682	13.055	15 + 16	NI	744.4348	11.996	9
Unid.[c]	437.18	——	15 + 16	NI	747.0369	11.996	9
NI	467.1200	13.345	11	KI	766.7021	1.617	9
ZnI	468.1444	6.655	14 + 15	KI	770.1093	1.610	9
ZnI	472.3474	6.655	14 + 15	OI	777.4083	10.742	
ZnI	481.1872	6.655	14 + 15	+OI	777.6305	10.741	9
HI	486.2681	12.749	14	+OI	777.7528	10.741	9
Unid.	487.6	——	14	NI	790.1155	13.927	9
NI	491.6312	13.202	14	+NI	790.1457	13.927	9
NI	493.6495	13.202	14 (+13)	NI	791.7596	13.924	9
OI	533.0581	13.067	14 (+13)	Unid.	804.3	——	9
+OI	533.0589	13.067	12 + 13	NI	818.7111	11.845	8 + 9
+OI	533.1164	13.067	12 + 13	+NI	819.0263	11.841	8 + 9
+OI	533.1173	13.067	12 + 13	NI	821.2972	11.841	8
+OI	533.2218	13.067	12 + 13	NI	821.8595	11.845	8
+OI	533.2224	13.067	12 + 13	NI	822.5389	11.838	8
NI	575.4095	14.000	12 + 13	NI	824.4655	11.841	8
+NI	575.4244	14.000	12	OI	844.8568	10.990	8
+NI	575.4873	13.995	12	+OI	844.8680	10.990	8
NI	577.7895	13.986	12	+OI	844.9079	10.990	8
+NI	577.8386	13.991	12	NI	857.0089	12.127	8
NaI	589.1583	2.105	12	NI	859.6361	12.123	8
NaI	589.7558	2.102	12	NI	863.1605	12.127	8
OI	615.7665	12.755	12	NI	865.8256	12.123	8
+OI	615.7675	12.755	11	NI	868.2666	11.765	8
+OI	615.7693	12.755	11	+NI	868.5788	11.758	8
+OI	615.8441	12.755	11	+NI	868.8535	11.754	8
+OI	615.8459	12.755	11	NI	870.5637	11.751	8
+OI	615.8482	12.755	11	NI	871.4096	11.754	8
				NI	872.1232	11.758	8

[a]In order $m = 10$ blended with 777 nm ghost. [b]Possible ghost of N 822 ($m = 8$). [c]Possible Zn 468.144 ($m = 14$) ghost.

1. Three-Dimensional Deconvolution: Fast Fourier Transform

The first approach investigated was a deconvolution of the image. By deconvolving the measured spectra with the point-spread function of the camera and convolving with a Gaussian PSF of FWHM = 3.0 pixels, the wings in the emission profile were removed. The PSF was broader than 2 pixels, conforming to the Nyquist sampling theorem constraint [7,8]. The result was very satisfying for higher echelle orders, because peaks to the left of Fig. 5 were well separated and the background had been removed. However, the lower orders gave negative intensities between the orders (Fig. 5, right). It was attempted to extract each order by summing all pixel intensities and setting a background level at the bottom of each interorder minimum. Unfortunately, the results for the low orders $m = 8$ and 9 were sensitive to the adopted definition of this background. The background still contained source emission. In addition, the results for the higher orders were noisy. Lines produced ghost images, and overall the noise was enhanced.

In addition to this, the SRC entry observations differed from those of calibration lamps by having emission lines in the images. Each emission line is a (instrumentally broadened) point source on top of a diffuse continuum emission. The FFT deconvolution algorithm produced rings around the line images, resulting in dips left and right of the center of each line in the extracted images. The rings appeared as soon as some flux was distributed around the line. The problem was important only for the strongest lines in the spectra from Zn, K, O, and N. To remedy this problem, the sampling theorem should be obeyed in the deconvolved image, and no smoothing applied to the point sources [7,8], which would naturally suppress the ringing around the lines and ensure that no bias will appear as a consequence of smoothing. By keeping the spatial resolution of the reconstructed image high, the effect of ringing was made less strong, but it was not fully avoided in the FFT method.

2. Two-Dimensional Estimation of the Background: PSF Fitting to the Orders

Subsequently, the use of a two-dimensional separation was investigated, recognizing that the background of a given order was

Table 5 Molecular band heads found in the spectra

Molecule	λ, nm, (vacuum)	Order	Notes
CN violet system ($B^2\Sigma^+$-$X^2\Sigma^+$)	386.10 (ν = 2-2)	17 + 18	Band head
CN violet system ($B^2\Sigma^+$-$X^2\Sigma^+$)	387.15 (ν = 1-1)	17 + 18	Band head
CN violet system ($B^2\Sigma^+$-$X^2\Sigma^+$)	388.34 (ν = 0-0)	17 + 18	Band head
N_2^+ 1$^-$ system ($B^2\Sigma_u^+$-$X^2\Sigma_g^+$)	388.4 (ν = 0-0)	17 + 18	——
N_2^+ 1$^-$ system ($B^2\Sigma_u^+$-$X^2\Sigma_g^+$)	391.40 (ν = 0-0)	17 + 18	——
CN Violet system ($B^2\Sigma^+$-$X^2\Sigma^+$)	418.1 (ν = 2-3)	16	——
CN Violet system ($B^2\Sigma^+$-$X^2\Sigma^+$)	419.8 (ν = 1-2)	16	——
CN Violet system ($B^2\Sigma^+$-$X^2\Sigma^+$)	421.5 (ν = 0-1)	16	Blended with NI lines
N_2 1$^+$ system ($B^3\Pi_g$-$A^3\Sigma_u^-$)	620–685 (ν = 3)	——	11 + 10
N_2 1$^+$ system ($B^3\Pi_g$-$A^3\Sigma_u^-$)	700–776 (ν = 2)	——	10 + 9
N_2 1$^+$ system ($B^3\Pi_g$-$A^3\Sigma_u^-$)	820–880 (ν = 1)	——	8
CO^+ (A-$^2\Pi_i$)[a]	396.42 (ν = 0-0)	17	——
C_3 ($^1\Pi_u$-$^1\Sigma_g^+$)[a]	404.98 (ν = 0-0)	17	——
CH ($A^2\Delta$-$X^2\Pi$)[a]	431.01 (ν = 0-0)	17 + 18	——
C_2 (A-$^3\Pi_g$) Swan[a]	473.5 (ν = 1-0)	14 + 15	——
C_2 (A-$^3\Pi_g$) Swan[a]	516.5 (ν = 0-0)	13	——
C_2 (A-$^3\Pi_g$) Swan[a]	563.5 (ν = 0-1)	12	——

[a]Not found.

the sum of the wings from all other orders. The images were well focused. Each image showed some amount of motion blurring during the 0.1 s. exposure, but the scattering function was well fitted by a Lorentz curve. The FWHM increased for higher orders. For Echelle097, the width of the lines was FWHM $= \sqrt{(-76.0 + 12.0 \times \mathrm{m})}$ pixels, with FWHM = 4.4 pixels for $m = 8$ and FWHM = 12.8 pixels for $m = 20$. It is now possible to subtract from each order the background contributed by all other orders. The integrated flux of each order was determined iteratively by fitting Lorentz curves to the mean data for pixels X = 597–603.

By adding the intensities over one FWHM centered around the order peak, the same overall shape of the spectrum was obtained as in a full 3-D deconvolution using the FFT algorithm, except for a positive residue at low intensity levels, but with a much better signal-to-noise ratio.

The 2-D fitting procedure does not have the problem of creating artificial features around the strong emission lines, but strong lines do leave residual features in adjacent orders. These residues were removed from the strong lines of oxygen, nitrogen, potassium, ionized calcium, and zinc.

B. Point-Spread Function

During the mission, distant artificial lights were observed to align the spectrum on the CCD, focus the camera, and determine the position of the source on the crosshairs of the coaligned pointing camera. These lights were located on aircraft hangars across Moffett Field, the location of the aircraft during instrument upload, at a distance of about 800 m. After the tarmac calibration tests, which used nearby calibration lamps, the camera was refocused on these hangar lights.

After focusing, the point-spread function (PSF, Fig. 6) was measured using an Ocean Optics HG-1 mercury argon line-emission calibration source, with an exit aperture of 3.0 mm, which was placed 3.0 ± 0.5 m away from the spectrograph, outside the aircraft at about 0 deg elevation. The lamp was observed at an angle of about 50 deg right of the boresight out of the window (with ECHELLE being mounted over the motor and wing edge). The camera was focused on the calibration lamp, which had an angular diameter of ∼0.06 deg. Each spectral line was an image of the source. Because the source was in the foreground, the source was slightly resolved by about 10 pixels, broadening the orders, but not affecting the PSF much outside the line center. These observations provided a good measurement of the PSF away from the line center, but needed sources in the far field to resolve the center. The hangar lights were too large, even at their distance. Instead, the point-spread function in the line center was measured from the shape of lines in the Sample Return Capsule spectra (Echelle097). The emission from the capsule was an unresolved point source. The core of Fig. 6 is a combination of vertical scans through a bright emission line, after subtraction of the sky background emission.

A Lorentz profile with FWHM = 4.0 ± 0.4 pixels, centered at the peak intensity and peak position of the line, was fitted to the point-spread function (Fig. 6, dashed line). The core of the curve was slightly narrower and the top of the underlying scattered light component was slightly broader than this function. Motion blurring and a resolved source will tend to broaden the peak, but the wings of the PSF remained unchanged.

C. Wavelength Calibration

The wavelength scale (Fig. 7) was calibrated by observing an Ocean Optics HG-1 mercury argon calibration lamp. Vacuum wavelengths for mercury and argon were obtained from the Kurucz tables [9]. The positions of the mercury and argon lines were measured in numerous calibration spectra (also from later laboratory measurements) to determine how the wavelength varied as a function of echelle order (in meters). For the final calibration, identified emission lines in the Stardust SRC entry data were used to make sure that the wavelength scale pertained to a source at near infinity. Independent wavelength calibration for the slit-based spectrometer (called SLIT) experiment [10], an optical-fiber-fed spectrograph, provided confirmation for the identification of features in the near-UV part of the spectrum. No significant variation in the wavelength scale was noticed between relatively nearby and distant sources.

The wavelength scale and the intercept were found to change linearly (Fig. 8) with the inverse of the echelle order for m = 8–20:

$$\lambda(\mathrm{nm}) = 1/(6.3398 \times 10^7 + 0.00015881 \times \mathrm{m}) + \mathrm{pixel}/(-0.043028 + 1.249 \times \mathrm{m}) \quad (1)$$

Emission lines that are found repeatedly in overlapping orders verified the result. The wavelength scale was robust, with no variation of the slope of the scale (nanometers per pixel) for a given order as a function of distance between source and camera (and consequential refocusing of the lens during each measurement), shown in Fig. 9, or as a function of the position of the source in the field of view.

The position of the spectrum on the CCD depended on the position of the light source in the field of view. The vertical position of the echelle order pattern on the CCD was identified by the intercept of the lowest order $m = 8$ (Y position in pixels, at $X = 1$), while the horizontal position of the orders was measured by determining the horizontal shift of the 777 nm line of oxygen relative to that observed in Echelle097 (X position in pixels). The positions of all orders and the wavelength for each pixel were defined by the calculated position of the order $m = 8$ intercept wavelength. Of course, this intercept changed with a changing position of the source in the field of view.

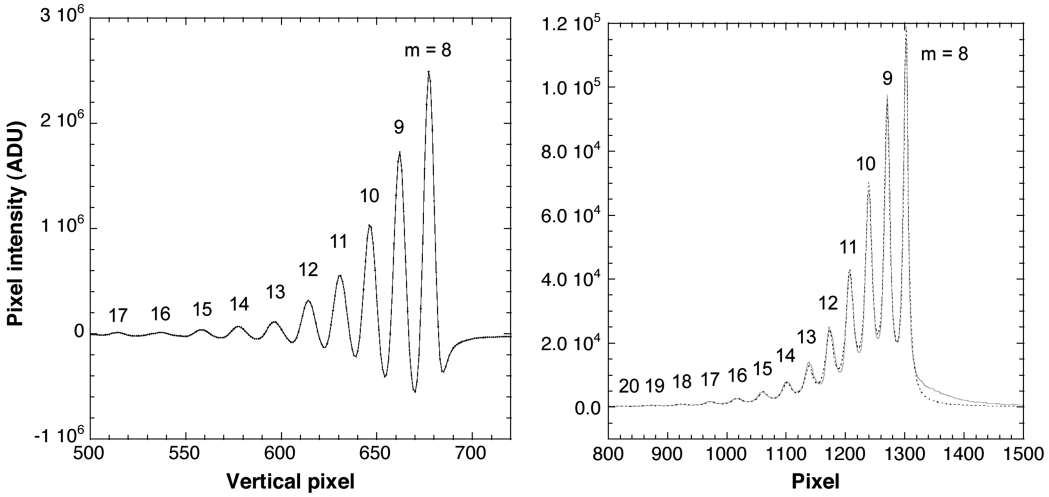

Fig. 5 Vertical (cross order) scan of tungsten calibration lamp spectra. Left panel: after deconvolution with a Lorentz profile and convolution with a Gaussian profile ($\sigma = 3$ pixels). Right panel: after fitting a sum of Lorentzian PSF (dashed line).

D. Spectral Response Calibration

During the mission, spectral response calibrations were made using two portable Ocean Optics LS-1-CAL tungsten calibration lamps, which came with a National Institute of Standards and Technology (NIST)-traceable [11] calibration curve provided by the manufacturer. The lamps had a small circular aperture, which functioned as a near point source when placed a few meters away. An Ocean Optics HG-1 mercury argon calibration lamp placed at the

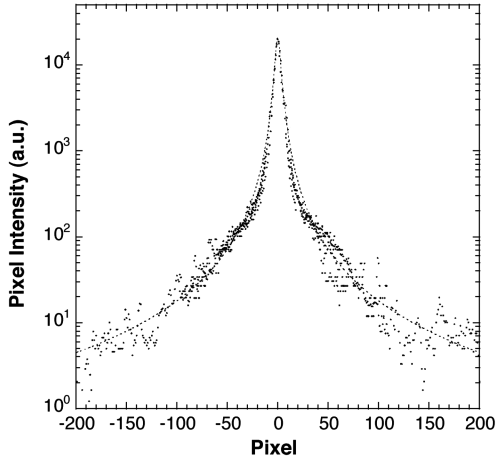

Fig. 6 Point-spread function derived from the shape of atomic emission lines. Note how bright lines have a diffuse glow of scattered light.

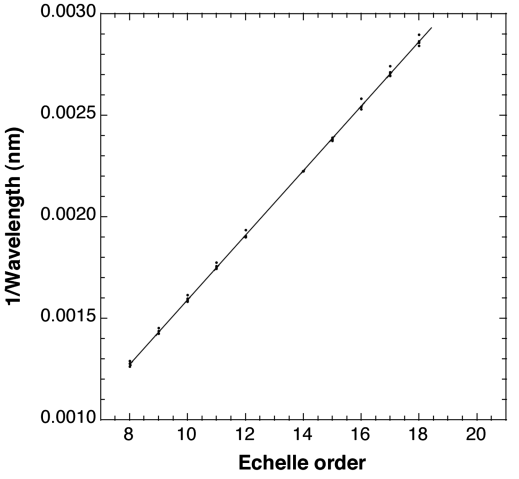

Fig. 8 Wavelength scale factor [Eq. (1)] as a function of echelle order (in meters).

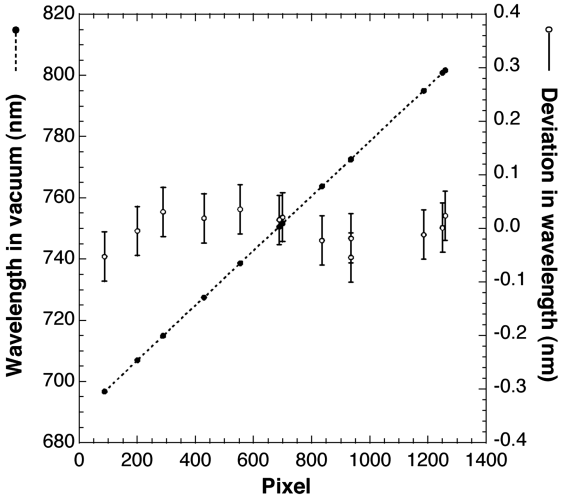

Fig. 7 Linear wavelength scale along one order ($m = 8$). The deviation from a straight line is shown as open symbols, with an expanded scale to the right.

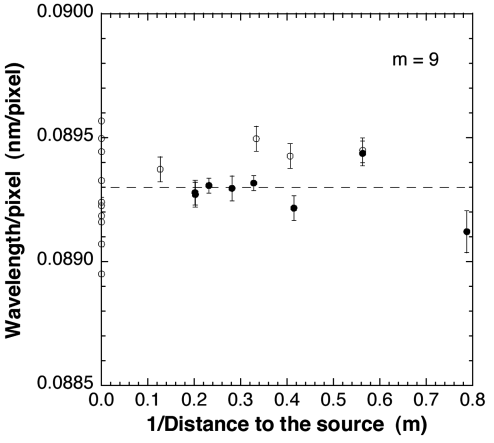

Fig. 9 Wavelength scale for order $m = 9$ as a function of inverse distance to the source; Stardust SRC (○) and from LSC207 lamp calibration (●).

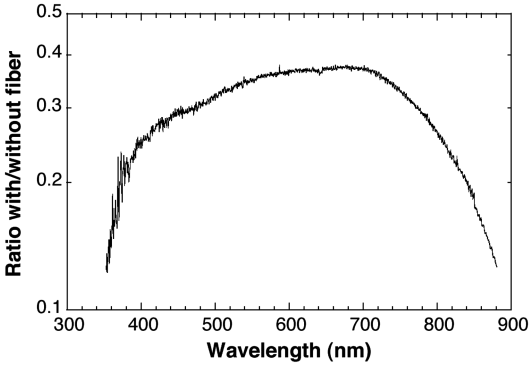

Fig. 10 Attenuation of flux detected by a spectrometer (10 nm resolution) from the LS-1-CAL calibration lamps with and without a connected fiber.

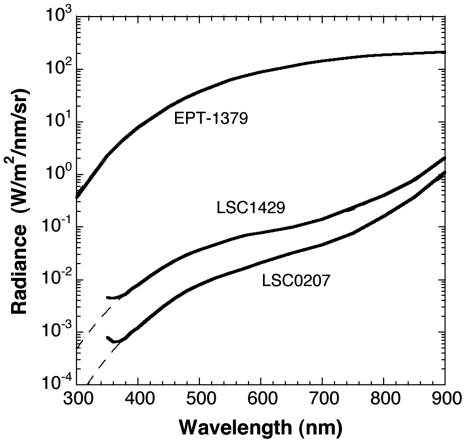

Fig. 11 Spectral radiance of calibration lamps.

same position as the tungsten lamp provided the wavelength calibration of the continuum emission (Sec. IV.C).

The measurements were repeated postflight using an Eppley Laboratory, Inc., calibration lamp, projected on a pinhole. By comparing the results, it was found that the factory-provided calibration curves for the Ocean Optics LS-1-CAL tungsten calibration lamps did not correspond to the observed emission when used in this manner. The discrepancy was caused by the use of an optical fiber to couple the light emitted by the lamp to the NIST-traceable calibrated spectrometer. Details of these calibrations are given in Appendix A.

Figure 10 shows the attenuation of the lamp flux with and without connecting an optical fiber to the lamp. The measured flux was also affected by the dimensions of the slit used in our spectrograph and by the diameter of the fiber used in the Ocean Optics-provided calibrations and its projection on the slit of their spectrograph. Ocean Optics used a spectrograph with a slit of 50 μm wide and 1 mm long, as did we. The fiber attenuation is a function of the cladding used and was reproducible. After correction for these effects, the spectral radiance for each of the calibration lamps is shown in Fig. 11 (see Appendix A).

In the case of the newly purchased LSC1429 lamp, used in tarmac calibrations, the radiance curve resembled a blackbody curve for the nominal filament temperature of $\sim$2800 K with dilution factor 5.4×10^{-4} (assuming emissivity of 1.0) below 650 nm wavelength, while some light was retransmitted at near-infrared wavelengths, adding (with scaling factor 1.46×10^4) a colder component with $T \sim 775$ K at higher wavelengths (dashed line Fig. 11). The older LSC0207 lamp had a cooler filament temperature of $\sim$2510 K up to 650 nm (dilution factor 4.1×10^{-4}) and the same level of excess emission with $T \sim 760$ K above that. The inherent precision is probably not better than 10%. In comparison, the spectral radiance of the Eppley lamp below 1000 nm resembled a blackbody curve with color temperature $T = 2730$ K, with an emissivity factor of 0.75. The inherent precision of this lamp is of order 1%, with an additional 1.6% from uncertainty in the lamp's current and the aperture's solid angle (total 1.9%).

E. Response Nonlinearity

Several problems from using different lamps at different distances from source to camera caused the response from the various calibration measurements to disagree. These issues are now addressed.

1. Sky Background

The stardust observations were taken against the night sky and consequently had a very low, nearly absent, sky background (Fig. 12). That is not the case for the tarmac calibration tests and some

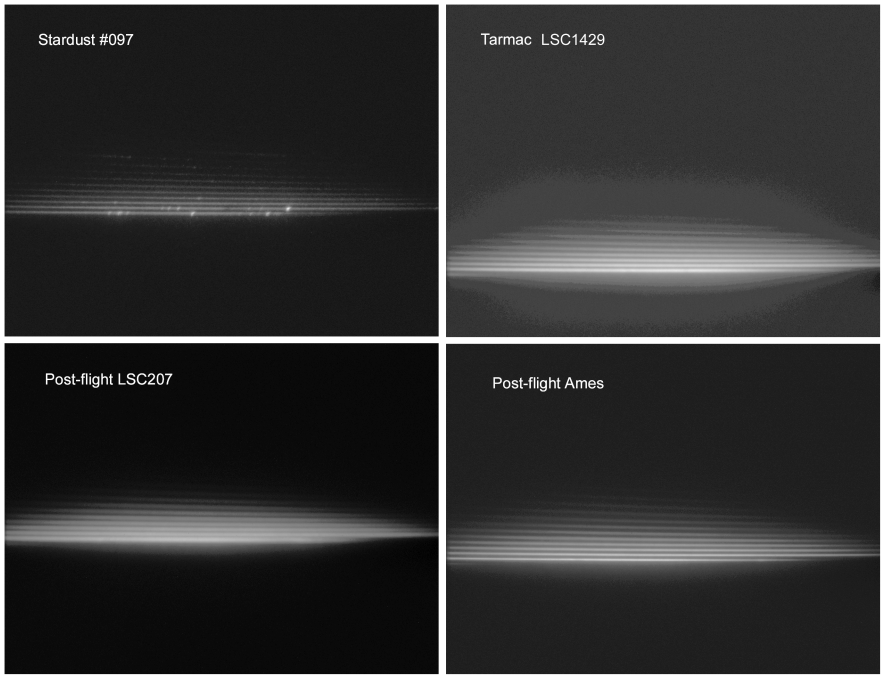

Fig. 12 Typical Stardust SRC spectrum (top, left) and tungsten lamp calibration spectra. Left: Individual lines are orders $m = 8$ (bottom, near IR) to $m = 17$ (top, near UV). The left images are shown at half true scale, and the intensity levels are adjusted in this picture to bring out the faint scattered light.

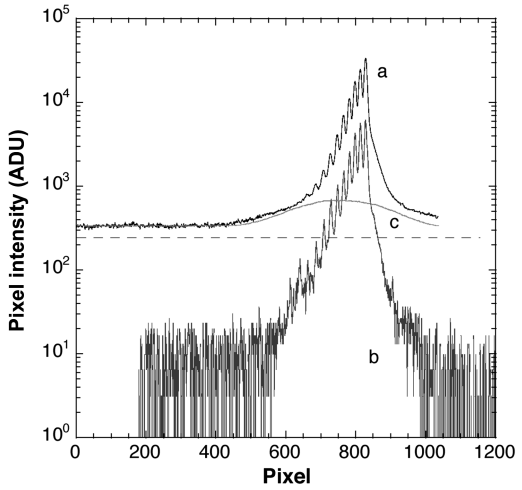

Fig. 13 Vertical scan of about 50 pixels wide across the peak intensity of each order in the Fig. 7 images: a) tarmac test, after subtraction of a dark frame, b) same for Stardust SRC spectrum (Echelle097), and c) sky background at tarmac.

of those done in the laboratory. The tarmac calibration measurements were made with the LSC1429 lamp positioned on top of a ladder at a distance of 3.0 ± 0.5 m outside the aircraft, about 50° to the right of the boresight direction. Because of nearby hangar lights and the bright city sky over Moffett Field (and due to scattering in the window), these tarmac calibration spectra had a high sky background (c in Fig. 13). The shape of the light distribution was a function of the dispersion of a diffuse background light and the vignetting in the camera. To remove this background, a background frame was subtracted from the spectra.

2. Nonlinearity in the Gain Setting

The response of the camera to different settings of the intensifier gain is not linear (Fig. 14). This has no consequence for the SRC entry observations, because the gain setting was not changed during the observation, but it does affect the laboratory calibrations.

A series of spectra were measured using the LSC0207 lamp in a laboratory setting on 8 February 2007, to discover that the response increased with an exponent 1.295, instead of 1.0 (Fig. 15). For this calibration, the lamp was placed at a distance of 194.75 in. from the front of the camera lens. Exposure time is 0.100018 s, CCD gain is 1.0, and gamma is 1.0, as for Stardust. The following measurements were made (each time the IG was set using the digital display on the camera control software), with subsequent settings of IG = 8000, 4000, 2000, 1000, 500, 250, 125, 75, 8000, 16,000, 22,000, 80,000,

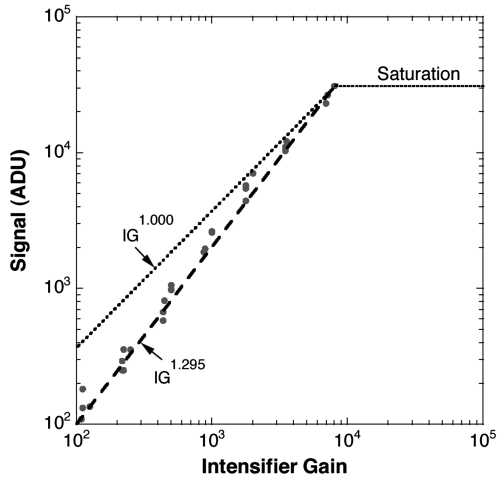

Fig. 15 Response of the camera as a function of the IG setting.

8000, 1000, and 500. Darks were measured by keeping the lamp on, but putting an obstruction in front of the lamp (IG = 8000). This was followed by observations of a HgAr line-emission calibration lamp (IG = 8000, 1000, 500, 100, and 80,000).

3. Nonlinearity of Intensified CCD

The linearity of the system was also tested by observing the same lamp at different distances from the camera and by comparing the response to individual pixels of images taken at different positions of the lamp (Fig. 16). All measurements were made with IG = 200. The result confirmed the prior measurements and showed that the nonlinearity was not merely due to the software gain setting.

The sensor was linear at least until (scaled) intensity level 10,600, with 65,532 being the maximum value, but deviated significantly above. This corresponded to original bits 1–10, with 11 and 12 slightly underestimated. Above a response of 10,600 (and below 65,532), the correction toward a linear response was

$$f_o = f \times (f/10600)^{0.333} \qquad f > 10,600 \tag{2}$$

This amounted to a factor of 2 correction at saturation and affected the brightness of the strongest oxygen and nitrogen emission lines in the later Stardust observations, which ended up spanning measured intensity levels from 10,000–50,000 on this scale (but did not saturate).

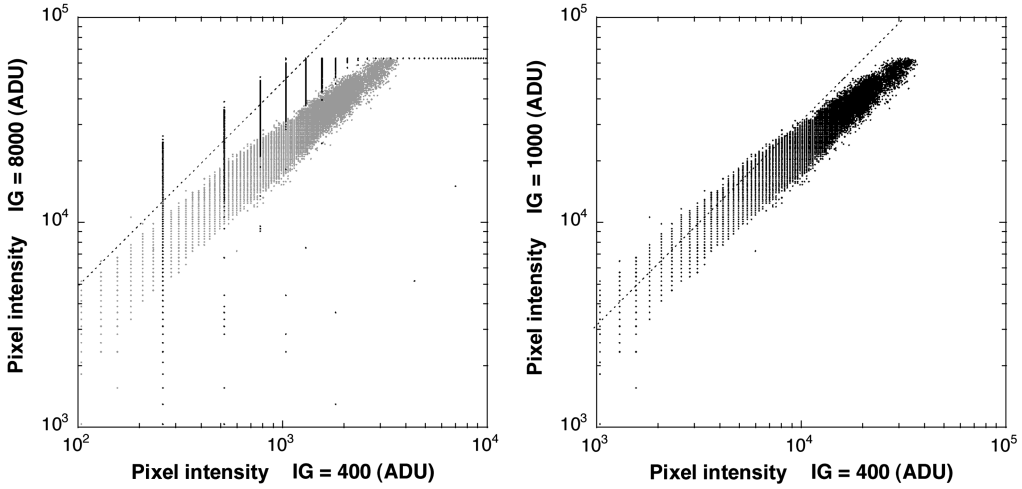

Fig. 14 Nonlinearity in the detector response. Pixel-to-pixel comparison (background subtracted) of a HgAr calibration lamp at different distances from the camera. Left figure shows the same data on a logarithmic scale. The dashed line has a slope with power 1.0.

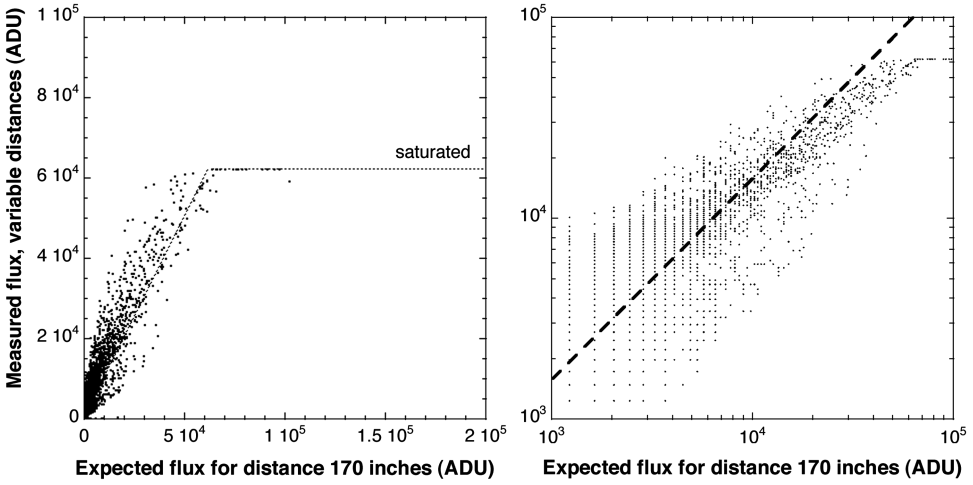

Fig. 16 Nonlinearity in the detector response. Pixel-to-pixel comparison of ARC lamp tungsten frames taken at different gain settings. Right image is superposed in light gray on the left image for comparison.

4. Instrument Vignetting as Function of Position of the Source

The pattern faded as a whole when the source was significantly outside the center of the field of view. The intensity of the overall pattern was tested as a function of position on the CCD (Fig. 17). The wavelength scale did not noticeably change. Moving the camera in the horizontal direction changed the vertical position of the pattern on the CCD (direction of order separation). Subsequently, moving the camera in the vertical direction, which was more difficult to control, changed the pattern in the horizontal (dispersion) direction.

These measurements were used to correct the overall pattern intensity as a function of the two position parameters. Note that this correction had little effect on the SRC entry observations, during which the capsule was kept close to one position near peak response (bar in Fig. 17). However, the vignetting is important for understanding the laboratory calibration measurements.

5. Flat Field

Finally, the camera was detached from the SE 200 spectrograph assembly and flat-field spectra were measured by pointing the bare intensifier (no lens) at an illuminated white wall, for different settings of the intensifier gain (Fig. 18).

These flat fields showed a vignetting from the housing of the intensified camera. This vignetting could be removed using a high-pass filter with a 90-pixel radius. The result was a flat-field image that corrected only for pixel-to-pixel intensity variations. Note that, at this time, there was also a faint ghost image of past bright light exposures during the postflight calibration measurements.

The influence of the flat field is mostly mitigated by averaging spectra along several rows across the order and because the spectra of individual observations are always at somewhat different positions on the CCD. As a result, any pixel-to-pixel sensitivity variations tend to average out. Data were reduced both with and without flat-field correction and showed little difference. Because of that, the flat-field correction was not included in the final reduction.

F. Blaze Function

The blaze function describes the shape of the spectral intensity in each order (Fig. 19). The theoretical blaze function of an echelle spectrograph with a plane grating used in near-Littrow mode is given by [18]

$$f(\lambda) = \sin^2(\pi\alpha X)/(\pi\alpha X)^2 \tag{3}$$

with

$$\alpha = 0.5 \quad \text{and} \quad X = m(1 - \lambda_c)/\lambda \tag{4}$$

where m is the echelle order number and λ_c is the blaze wavelength of that given order, which is the central wavelength at the peak of the order:

$$m\lambda_c = 2\Lambda \sin(\delta)\cos(0.5\theta_c) = \text{constant} = \kappa \tag{5}$$

Here, Λ is the groove distance, $1/\Lambda = 60$ lines/mm; δ is the blaze angle; and θ_c is the camera-collimator angle. Because $\lambda_c \gg 1$ nm, this simplifies to $\alpha = 0.5$.

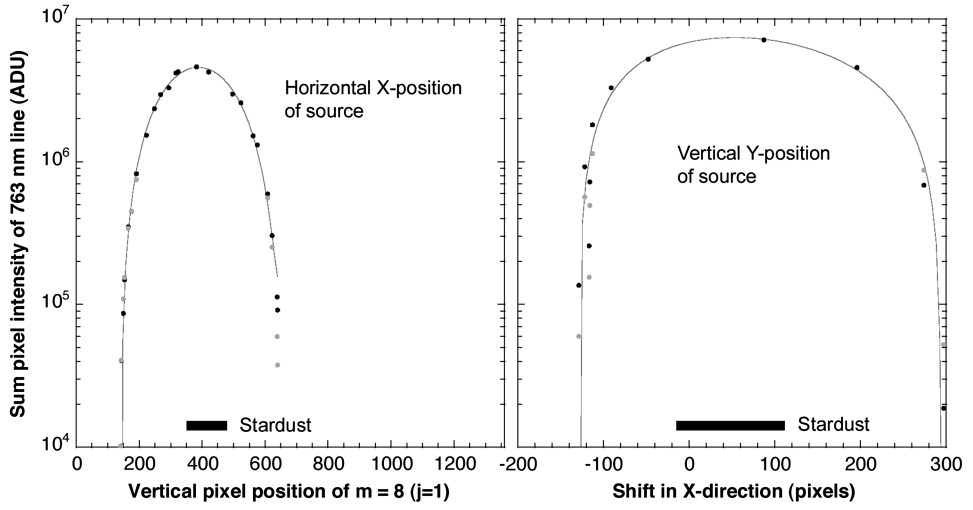

Fig. 17 Variation of intensity with changing position of the ECHELLE pattern on the ICCD.

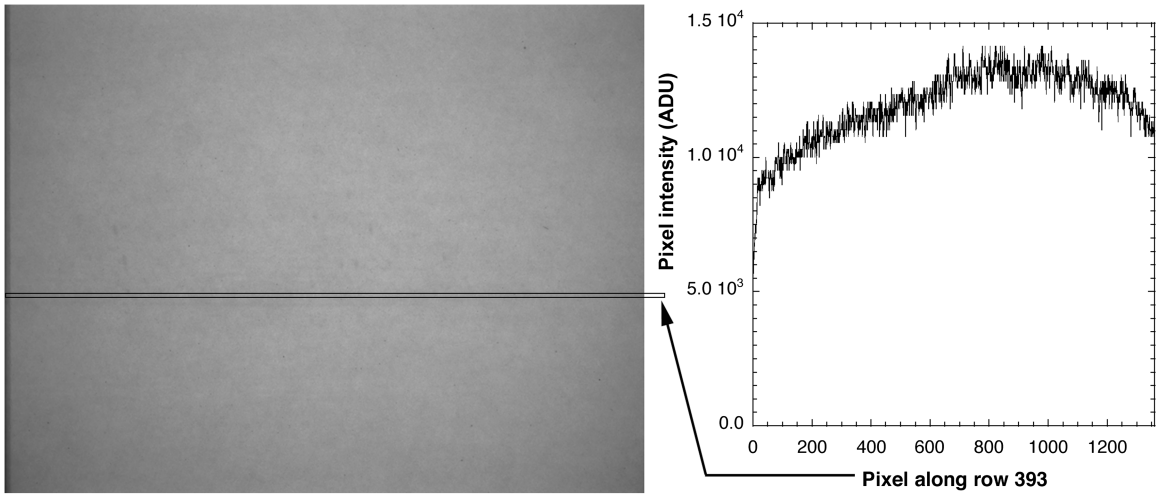

Fig. 18 Flat-field background. ICCD response to a plain illuminated surface. Right is a cross section along row 393.

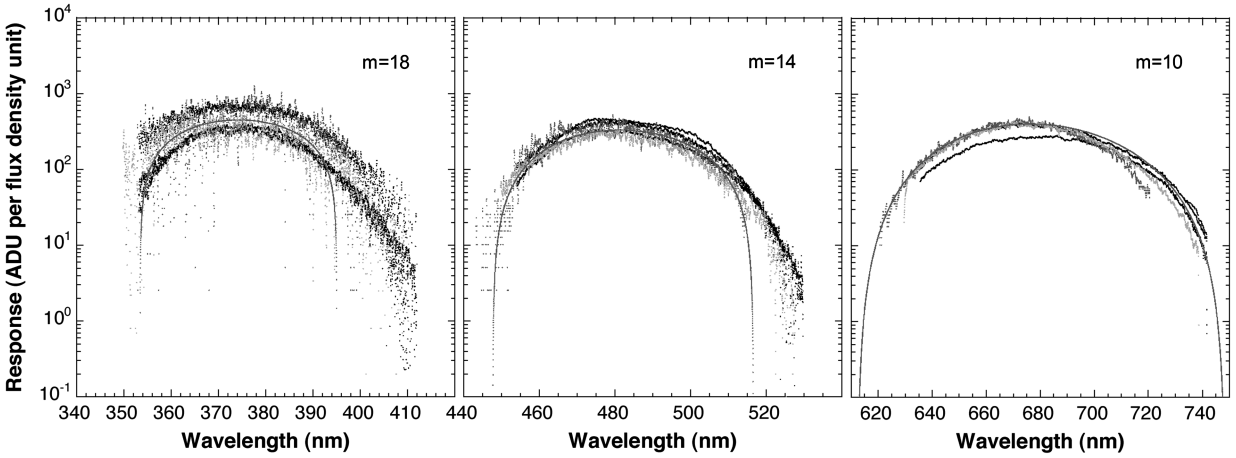

Fig. 19 Response curves for each order (in meters), derived by dividing the measured pixel intensity (ADU) by the calibration lamp flux density for ARC lamp (dark points) and LSC0207 and LSC1429 lamps (gray points). A response function was calculated based on the blaze function (solid line).

For $m = 8, 10, 12, \ldots, 20$:

$$f(\lambda) \sim \cos^2(\pi\alpha\kappa/\lambda)/(\pi\alpha\kappa/\lambda)^2 \quad (6)$$

For $m = 9, 11, 13, \ldots 19$:

$$f(\lambda) \sim \sin^2(\pi\alpha\kappa/\lambda)/(\pi\alpha\kappa/\lambda)^2 \quad (7)$$

The observed blaze functions (Fig. 19) are slightly wider than predicted by Eqs. (6) and (7). The width was adjusted by using the exponent for the cosine or sine as a variable (1.0–2.5). The center of the profile was matched by increasing or decreasing the blaze function (0–30). The best-fit result for the Eppley calibration lamp had $\kappa = 6700 \pm 146$ nm. This is in agreement with the factory value for the first-order blaze wavelength of $\kappa = 6700$ nm. The Eppley lamp gave a better fit for a value of $\kappa = 6722$. The result of representative fits is shown in Fig. 19. Subsequently, the orders were spliced for overlapping parts of adjacent orders.

G. Instrumental Spectral Response

Using these blaze functions, Fig. 20 shows the resulting flux detected from two calibration lamps in a laboratory setting. The calibration included effects from the instrumental response from lens transmittance, mirror reflectance, and ICCD responsivity. These tended to change gradually with wavelength within each order and were included in the blaze function fits. Only order $m = 8$ had a sudden drop in response toward long wavelengths. The response also has an irregularity just above 881 nm in this order.

After fitting a blaze function [Eqs. (6) and (7)] to the observed pixel intensities for each order, by adjusting the exponent (width of the function) and a scaling factor for the strength (Fig. 19), the resulting response curve integrated over all orders is shown in Fig. 21. Sharp features resulted from parts falling outside the CCD.

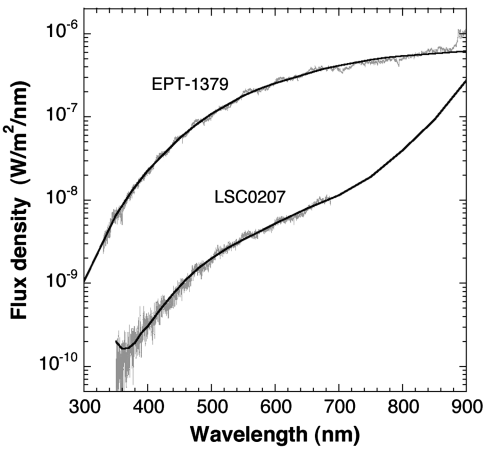

Fig. 20 Measured (gray) and calculated (solid line) spectral flux density for calibration lamps in a laboratory setting at $d = 7.9$ m (EPT-1379) and 5.3 m (LSC0207), no window.

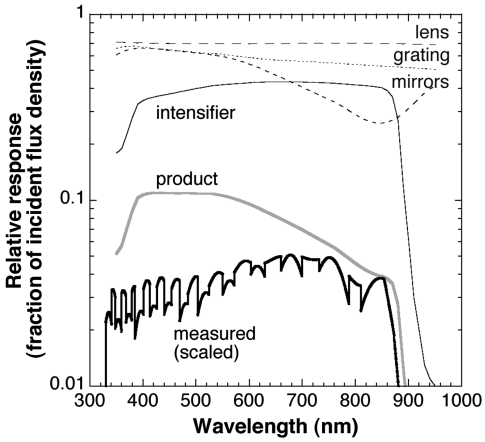

Fig. 21 Instrument response curve. Factory-provided response of individual components and their product. The measured response (not constrained vertically) is shown by a thick line.

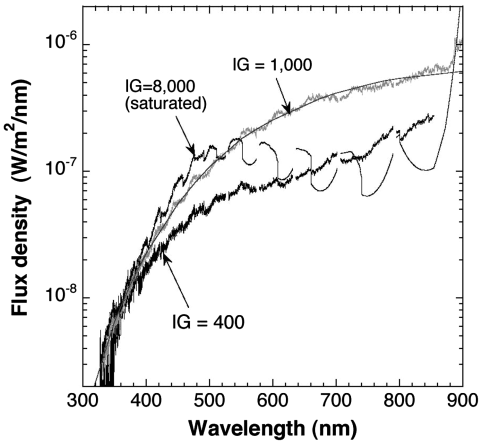

Fig. 22 Stability of response; under certain conditions, the long wavelength response becomes less.

The result is compared to that expected from the various components of the instrument. The sudden drop in response toward long wavelengths in $m = 8$ derives from the mirror reflectance and, mostly, from the photocathode response of the Extended-Blue Gen III intensifier.

In other aspects, the agreement between observed and expected response is not so good (Fig. 21). The intensifier was also expected to drop off (more gradually) toward shorter wavelengths, but that effect is not detected. The discrepancy between the product of factory-provided response curves and the measured curves may be mostly on account of incomplete knowledge of the component response curves and effects of vignetting in the camera.

Instrumental vignetting is also included in Fig. 20, as it is included in the empirical fit to the response of individual orders. Of course, vignetting is a function of position on the CCD, while the instrumental response curve and the blaze functions are wavelength-dependent instead. The combined effect can change the response from one situation to the next if the position of the source is different in the line of sight or if the source is in the near field.

H. Absolute Calibration of Spectral Response

The factor from relative response in Fig. 21 to absolute response equals $5.00 \pm 0.03 \times 10^{14}$ ADU/W/m^2/nm (where ADU is the analog-to-digital unit), based on the fit to the calculated Eppley lamp flux density. The flux at the position of the camera from the EPT-1379 Eppley lamp radiant source, observed through an aperture at a distance from the camera, was calculated from [12,13]

$$E_\lambda = L_\lambda^{\text{Eppley}} \times \phi_{\text{mir}} \times \Omega = L_\lambda^{\text{Eppley}} \times \phi_{\text{mir}} \times \pi(D/2)^2/d^2 \qquad (8)$$

where $L_\lambda^{\text{Eppley}}$ is the spectral radiance of the source (Table 1), ϕ_{mir} is the fraction of light lost by reflection from the mirror, D is the diameter of the aperture, and d is the distance from the aperture to the front of the camera lens. The response curve was absolutely calibrated by fitting to Eppley lamp series 803–902 spectra, with IG = 1000. The series 503–602 (IG = 8000) was saturated for all orders below $m = 15$ (Fig. 22). The series 903–1002 (IG = 400) had the same response as the IG = 1000 measurement for the higher orders ($m = 18$–20), but was less responsive for lower orders (Fig. 22).

In the same way, the spectral flux density for the recalibrated LSC0207 lamp was calculated from the flux curve of Fig. 11 using $E_\lambda = L_\lambda^{\text{O-O}} \times A^{\text{lamp}}/d^2$ (Appendix A). Care was taken to have the same instrument settings as during the Stardust observations (this caused order $m = 8$ to saturate, affecting $m = 9$ as well). The remaining orders match well to the calculated flux density, deviating on average within $\pm 11\%$ over the range measured. This calibration confirms that the IG = 8000 calibration with the Eppley lamp was reliable, while the IG = 400 measurement was wrong (Fig. 22). The reason for this discrepancy is not clear, but it may be related to instrument vignetting and slightly different observing conditions.

Similarly, the results from the tarmac tests with lamp LSC1429 matched the spectral shape of the individual orders (gray points in Fig. 19), but the distance between lamp and camera was not known accurately enough to improve the absolute response calibration.

I. Stray Light Rejection

The method used to extract the orders efficiently rejected stray light. However, the 2-D extraction procedure aligned the Lorentz curves to the peak position of the order on the CCD and therefore systematically positioned the curves on the peaks of shot noise signals in the absence of data. As a result, the reduction of the dark images gave a small positive signal (Fig. 23). This signal was measured from the background images taken immediately following the Stardust reentry data, before correction for extinction and window transmission. The signal is expressed by (in units of 10^{-12} W/m^2/nm

$$f_b = 5 + 40\sin^2(2\pi\alpha\kappa/\lambda) \qquad (9)$$

as shown by the solid line in Fig. 23. It was subtracted from all data at this stage in the reduction process.

J. Window Transmission

Particular to the Stardust observations was that the measurements were made through an aircraft window with a transmission curve, shown in Fig. 24. The window transmission curve of window 085 (Pyrex, high-efficiency antireflection coating) was measured over the

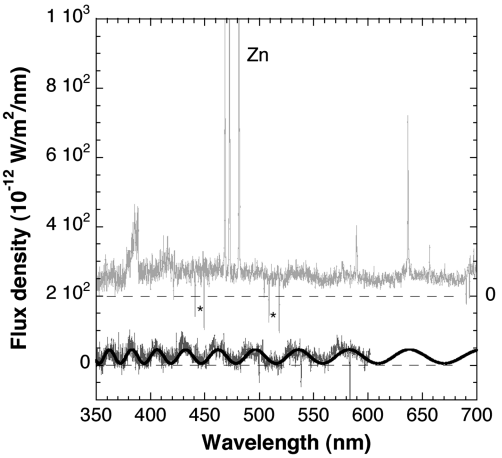

Fig. 23 No-signal background (bottom) compared to early ECHELLE data (top, offset for clarity), before extinction and window correction; ∗ = *Zn* line bleeding residues.

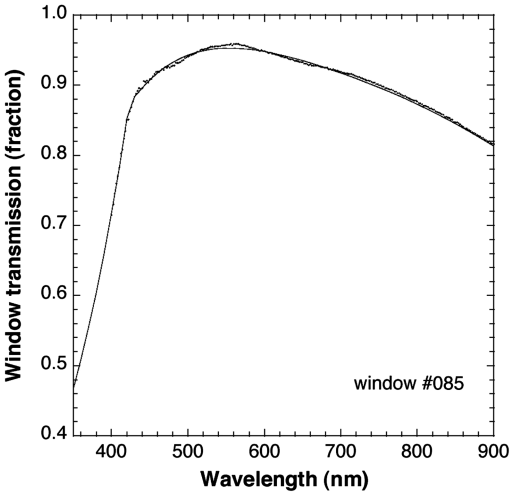

Fig. 24 Transmission curve for Pyrex window 085 (normal incidence, unpolarized light).

range of 400 to 2500 nm (room temperature, normal incidence) shortly after the prior November 2002 Leonid Multi-Instrument Aircraft Campaign mission in 2003. The transmission between 350 and 400 nm of window 099 was on file, which was of identical type and manufacturer. This measurement was made by Optical Coating Laboratory, Inc. (Santa Rosa, California) on 24 July 1979 (25°C, normal incidence).

The viewing geometry during the SRC entry observations was almost perpendicular to the window frame at boresight viewing, while at each given time the angle from the boresight (β) was known. It was assumed that the window absorption scales with the path length through the window plane, ignoring a change in reflection of the incident light. With the boresight at azimuth 307.15° E from N, the SRC was observed at angles changing from $\beta = -15$ to $-10°$. The corresponding correction factor $1/\cos(\beta)$ changed only from 1.035 to 1.015. The total window transmission was the transmission curve of Fig. 24 divided by this factor.

K. Atmospheric Extinction

Atmospheric extinction between capsule and airplane modified the spectra as well. The extinction was mostly due to Rayleigh scattering of oxygen and nitrogen molecules and the absorption of ozone. The oxygen A and B bands were also detected, but strong only in a small range of wavelength. Because of the aircraft altitude, there was only a small contribution from aerosols. We did not detect water vapor.

The near absence of water vapor and dust made it possible to reliably use the MODTRAN [14] (moderate spectral resolution atmospheric transmittance) algorithm and computer model to determine the level of Rayleigh scattering for different viewing direction geometries. The calculated atmospheric transmission was 0.37 at 350 nm, 0.53 at 400 nm, and 0.93 at 800 nm for Echelle011, and 0.44 at 350 nm, 0.61 at 400 nm, and 0.95 at 800 nm for Echelle097. Because of good transmission above 400 nm, the uncertain presence of aerosols did not affect these results by more than 10%.

The effect of atmospheric extinction on the shape of the spectrum is shown in Fig. 25 (gray line). The air mass was verified by the strength of the oxygen A and B molecular band absorption against the continuum of the capsule. The low level of water vapor present was verified from the strength of the 1.4 μm feature in other measurements. The influence of aerosols was the biggest uncertainty, but had a relatively small effect on the total extinction at all wavelengths.

V. Discussion of Errors

This final section concerns the estimates of measurement accuracy of the spectral radiant flux (flux density) entering the airplane window at a given time (expressed in $W/m^2/nm$) that were quoted earlier.

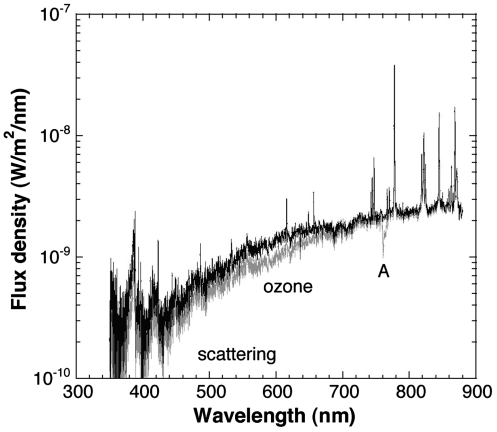

Fig. 25 Correction for atmospheric (telluric) extinction. Echelle spectrum 097 before (gray) and after (dark) correction for atmospheric extinction. The main sources are identified.

A. Time

The time of each spectrum in the image header is the moment of writing to the buffer and is accurate to ± 0.001 s. The whole spectrum was recorded simultaneously. The exposure time was 0.100018 s, which would put the middle of each time period 0.050 seconds before the time reported in the image header. The reported writing times fluctuated slightly. The time given in the final data release had this time subtracted and is accurate only to ± 0.01 s.

B. Wavelength

The position of the lines in the whole spectrum is related to how well the position of one of the stronger lines in the spectrum was measured. This determined the adopted shift of the pattern on the CCD. For a typical accuracy of ± 0.7 pixels, this amounted to ± 0.07 nm at $m = 8$ and ± 0.03 nm at $m = 18$. In reality, the error was larger, due to motion blurring from tracking of the meteor in the sky, and small deviations from Eq. (1) are due to the imaging optics. Typically, this limits the accuracy to about 0.25 FWHM, or $\Delta\lambda = \pm 0.11$ nm at $m = 8$ and $\Delta\lambda = \pm 0.30$ nm at $m = 18$.

C. Flux

1. *Flux Scale*

From a fit of the observed spectrum to that of the Eppley lamp, the random error in the calibration factor 5.00×10^{14} ADU per $W/m^2/nm$ (which determines the vertical alignment in Fig. 17) is $\sigma = \pm 0.45$, from the random deviations of each data point for the intermediate orders, with the standard error in the mean being only ± 0.005 of this value (0.06%). The Eppley lamp measurement itself had a random uncertainty of about 1.9%, dominating the calibration error.

Systematic errors are probably much larger. Given that these lamp calibrations were done in a laboratory setting some time after the entry observations, systematic errors could have arisen from differences in lens focus (near-field measurement), in the operation temperature, in the gain setting (although not changed between Stardust and postflight Eppley lamp measurements), from varying reflectivity of lens surfaces (although instrument was kept free of dust), or from electronic stability of the camera system.

There is a 0.3% difference of the blaze constant between laboratory calibrations and that during the Stardust SRC observations. The temperature of the optics system can have affected the blaze constant of the camera by expanding or contracting the grating, changing the distance between grating and prism, or changing the position of the detector plane. The spectrometer was not kept at a constant temperature and it cooled during the mission from being mounted on a platform directly attached to the window frame

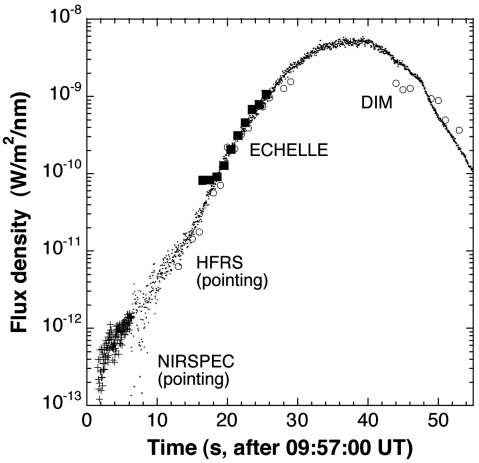

Fig. 26 Stardust SRC radiative flux at 548 nm wavelength as measured at the aircraft (corrected for atmospheric extinction). ECHELLE data (squares) are compared to other broadband measurements of SRC brightness that were independently calibrated against background stars.

(Fig. 2). The measurements onboard the aircraft were performed in an equilibrated temperature environment, due to the time it took to fly from Moffett Field in California to the observing site near the western border of Utah. The temperature of the support structure holding the camera could have dropped to close to 10°C, from a typical room temperature of 25°C. This is only based on the fact that the instrument felt cold to the touch and no water vapor had condensed on it. However, fused silica, the substrate of the grating, has a very low thermal expansion coefficient of $(5.5 \times 10^{-7})/°\mathrm{C}$. Hence, the substrate grating would only account for an $8 \times 10^{-4}\%$ change.

Some guidance to these errors comes from comparing the absolute flux scale to results with other lamps. Calibration against the LSC0207 lamp resulted in agreement with the Eppley lamp in the 500 to 660 nm range to $0.28 \pm 0.06\%$, but with standard deviation of 7.6% from one pixel to the next (6% of which is noise in the data). Hence, imprecise matching of the blaze function (by forcing calibration lamp and Stardust SRC entry observation blaze functions to be the same) is the dominant uncertainty.

Independent flux calibration also came from the star background. Other instruments measured the intensity of stars at the same time as measuring the (broadband) intensity of the Sample Return Capsule [12,13,15]. Figure 26 shows the comparison. The reported flux was that just outside the window of the aircraft with atmospheric extinction removed. Because stars and SRC were observed in the same small field of view, both were affected in the same way by atmospheric extinction. All data were normalized to the flux at 548 nm (visible). Open circles were derived from imaging data obtained with a digital imaging (DIM) camera [15], calibrated against Mars. Smaller dots were from intensified near-infrared spectrometer (NIRSPEC) [12] and low-light-level, high-frame-rate spectrograph (HFRS) [13] video cameras used for pointing, calibrated against background stars. These have a wider response than the green color band of the DIM camera. The HFRS pointing camera was also saturated past 19:57:20 UTC, but the bloomed images were corrected for saturation by matching to data measured by the unsaturated HFRS spectra (adjusting one free parameter that described the $1/e$ level of saturation) [13].

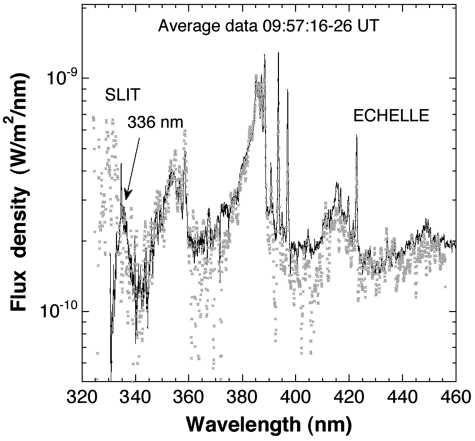

Fig. 28 Comparison with SLIT data (Winter and Herdrich [10]) for average over period 09:57:16.0–26.0 UTC [10].

Solid squares show that the ECHELLE fluxes at 548 nm, calibrated from laboratory measurements. The median deviation from the exponential trend in flux density shown by the DIM camera is $4.4 \pm 4.7\%$, in good agreement, while individual 1-s-averaged ECHELLE spectra scatter around this median value with a standard deviation of 15%.

The Stardust observations are also affected by possible systematic errors from uncertainties in the distance to the capsule, the atmospheric extinction in the line of sight, and the window transmission. These do not show up in the above comparison, because all data for a given point in time are corrected in the same way. The atmospheric extinction and window transmission are more uncertain toward short wavelengths. The uncertainty in atmospheric extinction could contribute an error of order $\sim$10%.

2. *Flux Density of a Given Spectral Line*

The artifacts from the imperfect correction of individual echelle orders and the choice of background correction introduced the biggest systematic uncertainty in the flux at a given wavelength. The calibration was redone independently for Echelle numbers 097–100, two years after the March 2008 reduction (February 2010 reduction),

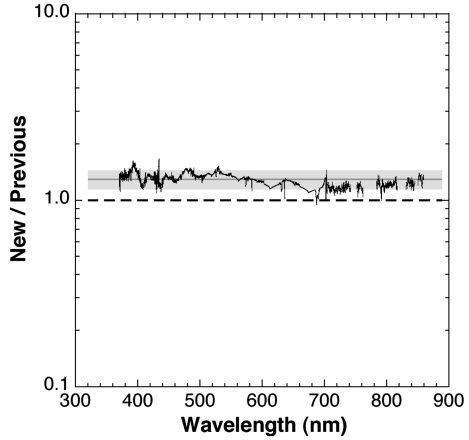

Fig. 27 Ratio of flux density, results from independent data reductions for ECHELLE frame numbers 091–100 (February 2010 versus March 2008). The gray bar indicates an uncertainty of ±10%.

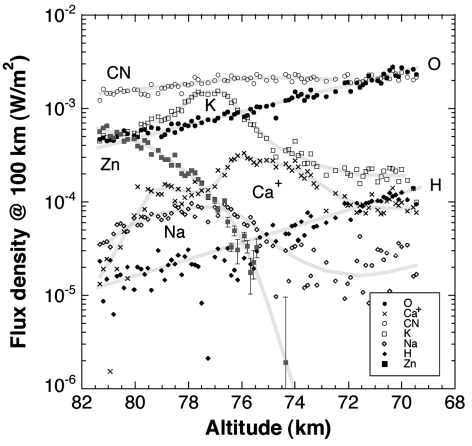

Fig. 29 Variation of integrated line intensity with stardust altitude (expressed as a flux density seen from 100 km distance).

and the ratios of the mean data for these two results are compared in Fig. 27.

The latest data calibration increased the flux density values by a factor of 1.30 (gray line in Fig. 27). In addition, the slightly different choice of the response for each order caused individual flux density values in the new solution to deviate by up to $\pm 10\%$ from previous results.

3. Flux Density at Short Wavelengths

Figure 28 compares the ECHELLE data (February 2010 data, solid line) to those of the SLIT instrument (March 2008 data), shown by gray crosses [10]. The extrapolation of the instrument response and window transmittance, assuming an exponential dependence below 350 nm, results in good agreement with SLIT down to a wavelength of 336 nm.

VI. Conclusions

The use of a slitless miniature echelle spectrograph for flux measurements of the reentry of a space vehicle has been demonstrated. The pointing and tracking method worked well. A process has been found to extract the flux from individual echelle orders to good accuracy for determining relative flux from one spectrum to the next. The new flux calibration increased the March 2008 flux density scale by a factor of 1.30. With this, an absolute calibration of the data to accuracy of better than 20% in flux density was achieved at 548 nm. The flux scale agrees to within 10% with independently calibrated data.

The use of more suitable calibration lamps can, in principle, reduce the accuracy of the data to better than 5% [16]. The instrument is sensitive enough to use background stars and planets as suitable calibration standards in the far field. Gain-setting changes can now be taken into account. Emission lines in the capsule's radiation provided an internal calibration of wavelength. Note that this may not always be the case.

The results presented here are available for interpretation. The data provide a record of continuum emission, presumably from the hot surface of the capsule, of air plasma emissions, and of line emission from a number of ablating compounds. These observations provided detailed insight into the physical conditions during entry, and the results were used to validate models of reentry processes [17]. Other observations remain to be explained. The ablation of the white paint layer is well documented. While the air plasma 777 nm line intensity of oxygen (O) increased exponentially with decreasing altitude, Zn, Na, K, and Ca^+ from a paint layer were ablated sequentially in that order (Fig. 29). The observations also present data on the ablation of PICA in the form of H and CN emissions. Their measured altitude-dependent intensity is a complicated function of chemistry and excitation conditions in the flow.

These spectroscopic observations of the Stardust Sample Return Capsule entry are expected to remain a unique data set for some time into the future. Opportunities to study sample capsule reentries under similar unique circumstances are rare. The observational data and the calibration files were archived for this purpose. The archived raw spectral images pertain to instrument definition tests and preflight tests on the tarmac before takeoff, the observations of the Stardust SRC entry, and the postflight tests. The present paper serves to document these files.

The ECHELLE instrument has demonstrated capability for future sample return capsule reentry observations, such as the return of the Hayabusa Sample Return Capsule in June 2010. Because it is a slitless instrument, it was also used to study the presence of metal atom line emissions in more complicated assemblies of point sources during destructive reentries, such as that of the automated transfer vehicle in September 2008.

Appendix A: Responsivity Calibration

I. EPT-1379 Calibration Lamp

A calibrated spectral radiance lamp by Eppley Laboratory, Inc. (no. 1379) was provided by NASA Ames Research Center (ARC) on 18 April 2006. The lamp had been recalibrated against NIST standards on 22 March 2006, between 225 and 2400 nm, which is traceable to a NIST standard (Table A1) [11].

The 6 V (228 W) lamp was operated at 38.000 ± 0.001 A. The filament of the Eppley lamp was viewed indirectly by means of a collimating mirror that projected an image of the filament on a blackened aluminum aperture plate with a small hole, which covered a small part of the filament wire. The mirror reflectance was described by ($\lambda < 1200$ nm) $\phi_{\text{mir}} = 0.875$ plus a Lorentz-shaped absorption centered at 850 nm, with depth of 0.050 and width of FWHM= 250 nm.

The aperture plate was placed at the focal plane of the mirror. The hole diameter of the aperture was 0.0189 ± 0.0001 in. (early measurements through a 0.0399 in. aperture were too bright). The diameter of the aperture was measured with a microscope on 21 April. Because of the high intensity of the lamp, the illuminated aperture was placed at a large distance from the front of the lens of the spectrograph, measured at 311.25 ± 0.25 in. (7.9 m) using a metal tape, for a solid angle of $\Omega = 2.896 \pm 0.015 \times 10^{-9}$. Room temperature was 72°F.

Initial measurements were made at an intensifier gain of IG = 8000, followed by an HgAr lamp held immediately behind the aperture, and background by closing the aperture. An effort was made to align the image on the CCD, to correspond to that during the SRC observations. The effect was also tested of having the source low in the field of view and high in the field of view. A second series

Table A1 EPT-1379 (Eppley) lamp, spectral radiance when operated at 38.000 A dc (mirror reflectance not included)

λ, nm	Radiance, $W/cm^3/sr$
225	3.899
230	5.387
240	10.59
250	20.48
260	38.92
270	70.56
280	122.2
290	200.1
300	318.0
325	878.7
350	1.973e3
375	3.882e3
400	6.816e3
450	1.674e4
475	2.399e4
500	3.267e4
550	5.416e4
575	6.500e4
600	7.627e4
654.6	1.025e5
675	1.119e5
700	1.226e5
750	1.417e5
775	1.503e5
800	1.560e5
900	1.779e5
1050	1.790e5
1100	1.748e5
1200	1.638e5
1300	1.481e5
1550	1.080e5
1600	1.007e5
1700	8.765e4
1800	7.600e4
2000	5.708e4
2100	4.936e4
2150	4.619e4
2175	4.450e4
2330	3.575e4
2400	3.251e4

of measurements were made with gains of 1000 and 400, all with the 0.0189 in. aperture. Further measurements were made at IG = 8000, followed by dark frames at this gain setting.

II. LSC1429 Calibration Lamp

During the mission, calibration measurements were made using a portable LS-1-CAL tungsten calibration lamp (model number LSC1429), which came with a NIST-traceable calibration curve provided by the manufacturer Ocean Optics (Table A2). According to the factory, the lamp used a long-life 6.5 W (5 V, 1.3 A) 2800 K color temperature halogen tungsten bulb, with the filament in a glass housing that cuts off light below 360 nm. The lamp decayed at a rate of about 0.1% per hour of operation, with decreasing color temperature, and needed about 20 min of operation for stable (within ~0.2%) output. A unique aspect of this lamp when used without a fiber was that it had a small circular aperture, which functioned as a near point source when placed a few meters away.

The LS-1-CAL lamp consisted of a tungsten filament and a block of Teflon placed in front of the filament. The Teflon acted as a Lambertian diffuser, where the intensity of the light fell off with the cosine of the observation angle to the surface. The radiance was independent of viewing direction. In this case, the geometric dilution for offaxis viewing was compensated by the scattering properties of the surface [18,19]. Hence, the incident power of the lamp was distributed uniformly over a 2π solid angle, diluting the light. In front of the Teflon block was a standard SMA 905 connector for optical fibers with an opening aperture of diameter $D = 3.0 \pm 0.1$ mm when the fiber was disconnected. When in use, the optical fiber was positioned close enough above the Teflon block so that the luminous area of the Teflon fully illuminated the opening angle of the fiber. The cone acceptance angle 2θ (whereby solid angle $\Omega_{NA} = 2\pi(1-\cos(2\theta/2)) = 0.154 \pm 0.028$ sr) was determined by the numerical aperture (NA) of the fiber: $\theta =$ invsin (NA). The factory-provided lamp calibration curve ($E^{O\text{-}O}$ in Table A2) was for a numerical aperture of NA $= 0.22 \pm 0.02$ fiber and, specifically, for a bare (no collimation optics or integrating sphere) optical-fiber diameter of 50 μm and a fiber length of 1 m.

III. LSC0207 Calibration Lamp

An older (many hours of operation) Ocean Optics LS-1-CAL calibration lamp (LSC0207), owned by the author, was used for postflight calibrations. The LSC0207 lamp was observed in a laboratory setting on 9 March 2006, now taking care to position the wavelength calibration source at the exact position of the tungsten lamp. An exposure time of 0.100018 s was used, the same as that during the Stardust SRC entry observations. The 1×1 binning and the CCD gain of 1.00 were also unchanged. The intensifier gain was adjusted to match the level of exposure.

Initial measurements were for IG = 8000, but those saturated the lower orders. A second series was for lower IG = 400. The measurement also included HgAr lines, flat-field frames, and dark frames.

The LSC0207 lamp response curve was recalibrated by Ocean Optics on 15 June 2006 (Table A3). During calibrations, the room temperature was reportedly 66°F and humidity was 57%. Standards used to calibrate this lamp included the HR2000CG-UV-NIR OOI50013 spectrometer (last calibrated on 15 June 2006) and the HR2000CG-UV-NIR OOI50014 spectrometer (also last calibrated on 15 June).

The recalibrated lamp was used to calibrate the ECHELLE spectrometer on 11 July. The lamp was positioned at a distance of 99.0 in. from the front of the lens to the Teflon surface of the lamp. Measurements were made at exposure times of 0.100018 s, CCD gain of 1.0, binning of 1×1, and intensifier gain of 8000, as during the SRC reentry observations, and for lower IG = 800. Care was taken to match the position of the spectrum on the CCD to that of the capsule's spectra. Dark frames at IG = 800 were made by covering the lens and were repeated for IG = 8000. HgAr measurements were made by replacing the LS-1-CAL lamp for an HgAr calibration source at the same position. The diaphragm of the lens was set to one stop down from open, just as during the Stardust observations.

Again, the source was in the foreground, creating a broad dispersion of light at the peak of the orders. The lens focus was adjusted to account for the closer distance to the lamp. The measurement was repeated on 11 November, with the source at a larger distance of 209 in. (at gain IG = 8000). Dark frames (sky

Table A2 LSC1429 continuum lamp calibration curve[a]

λ, nm	$E^{O\text{-}O}$, μW/cm^2/nm	Radiance, W/m^2/nm/sr
350	0.0075725	0.00455
360	0.010419	0.00440
370	0.013953	0.00471
380	0.017387	0.00527
390	0.023690	0.00665
400	0.030628	0.00788
420	0.049134	0.0117
440	0.073528	0.0167
460	0.10310	0.0227
480	0.13953	0.0297
500	0.17948	0.0365
525	0.23910	0.0460
550	0.30800	0.0571
575	0.38498	0.0694
600	0.43596	0.0773
650	0.56165	0.0983
700	0.79983	0.140
750	1.1824	0.235
800	1.6019	0.396
850	2.1696	0.783
900	2.9435	2.078
950	3.8239	(4.13)
1000	4.7443	(8.29)
1050	5.3132	(15.55)

[a]For each wavelength (in nanometers), Ocean Optics provided calibration curve for spectral irradiance $E^{O\text{-}O}$ for a 50 μm fiber attached (see text) and that calculated here for spectral radiance with no fiber attached.

Table A3 LSC0207 continuum lamp calibration curve[a]

λ, nm	$E^{O\text{-}O}$, μW/cm^2/nm	Radiance, W/m^2/nm/sr
350	0.0013292	0.000799
360	0.0015408	0.000651
370	0.0019639	0.000663
380	0.0025465	0.000771
390	0.0035909	0.00101
400	0.0047028	0.00121
420	0.0081166	0.00193
440	0.013148	0.00298
460	0.020002	0.00441
480	0.028651	0.00610
500	0.038923	0.00792
525	0.054899	0.0106
550	0.072108	0.0134
575	0.091928	0.0166
600	0.11773	0.0209
650	0.18078	0.0316
700	0.26047	0.0456
750	0.38250	0.0759
800	0.63980	0.158
850	1.0257	0.370
900	1.5593	1.10
950	2.2546	(2.13)
1000	3.1992	(4.44)
1050	3.9371	(8.60)

[a]For each wavelength (in nanometers), Ocean Optics provided calibration curve for spectral irradiance $E^{O\text{-}O}$ for a 50 μm fiber attached (see text) and that calculated here for spectral radiance with no fiber attached.

background) were taken by blocking the lamp from direct viewing.

IV. Recalibration of LS-1-CAL Lamps

The problem with this use of the LS-1-CAL lamps was that the factory-provided response curve did not apply. This curve was based on the use of an optical fiber guiding light into a calibrated spectrograph. The diameter of the fiber compared to the size of the spectrometer entrance slit mattered, as did the wavelength-dependent attenuation. The opening angle of the fiber matched that of the spectrograph used to make the calibrations.

To obtain the correct lamp response in the absence of a fiber, the LSC1429 and LSC0207 lamps were recalibrated by comparing the measured flux with and without the fiber in a laboratory setting using an Ocean Optics SD2000-TR-VIS spectrometer with a spectral resolution of 10 nm and a range of 350 to 1100 nm. Repeated measurements varied by $\pm 17\%$ (1σ), a combination of spectrometer and lamp instabilities and changes in the geometry when the lamp–spectrometer distance was changed.

The ratio of measured flux density with and without a fiber showed a strong wavelength-dependent function $\phi_\lambda^{\text{att}}$, with a shape reminiscent of that of fiber attenuation, but strong for such a short fiber. This included a loss of light from the smaller illuminated area of the spectrometer's slit. The opening aperture of the spectrograph without fiber was $A^{\text{slit}} = 1000 \times 50 = 50,000$ km^2, while the fiber opening aperture was $A^{\text{fiber}}\pi(50/2)^2 = 1964$ km^2 (assuming it is positioned well in front of the spectrograph slit). Hence, the fiber only covered a fraction: $A^{\text{fiber}}/A^{\text{slit}} = 0.03928$.

The spectral radiant flux (power) received at the spectrometer slit from the surface emitting with spectral radiance L_λ^{lamp} through a fiber is [18,19]

$$\Theta_\lambda^{\text{slit}} = L_\lambda^{\text{lamp}} \times \phi_\lambda^{\text{att}} \times A^{\text{fiber}} \times \Omega^{\text{NA}} \tag{A1}$$

The flux density (irradiance) at the slit opening, provided by Ocean Optics (Tables A1 and A2), is $E_\lambda^{O\text{-}O} = \Theta_\lambda^{\text{slit}}/A^{\text{slit}}$, where now $A^{\text{slit}} = A^{\text{fiber}}$. In the absence of a fiber, at a distance d from the surface of the lamp (A^{lamp}), the spectral radiant flux received at the lens opening is

$$\Theta_\lambda^{\text{lens}} = L_\lambda^{\text{lamp}} \times A^{\text{lamp}} \times \Omega^{\text{lens}} \tag{A2}$$

The solid angle of the lens as seen from the lamp surface is simplified here as (where r is the radius of the lens) [18,19]

$$\Omega_{\text{lens}} = 2\pi(1 - \cos[\text{invtan}(r/d)]) \sim \pi(r/d)^2 = A^{\text{lens}}/d^2 \text{ sr} \tag{A3}$$

The approximation is good to about 0.1% in our case. Here, $A_{\text{lens}} = \pi r^2$ is the surface area of the lens, with radius r in the same length unit as distance d, and $A_{\text{lamp}} = \pi(D/2)^2$ is the surface area of the SMA 905 connector aperture. The flux density at the lens opening is $E_\lambda^{\text{lens}} = \Theta_\lambda^{\text{lens}}/A^{\text{lens}}$, or

$$E_\lambda^{\text{lens}} = (E_\lambda^{O\text{-}O}/\phi_\lambda^{\text{att}})/\Omega^{\text{NA}} \times A^{\text{lamp}}/d^2 = L_\lambda^{\text{lamp}} \times A^{\text{lamp}}/d^2 \tag{A4}$$

The radiated power per unit area and per unit solid angle (units of W/m^2/nm/sr) emitted by the lamp (radiance) L_λ^{lamp} can be compared to Planck's law for the spectral radiance of a blackbody at thermal equilibrium temperature T:

$$L_\lambda^{\text{BB}} = 2hc^2/\lambda^5 \times 1/(e^{hc/\lambda kT} - 1) \tag{A5}$$

The resulting lamp radiance L_λ^{lamp} in the absence of a fiber is listed in Tables A1 and A2. The systematic error dominated the uncertainty in the result ($\sim$15%). Uncertainties originated also from the adopted NA of the fiber (and from the resulting Ω_{NA}), from the diameter of the SMA 905 connector, and from the slit and fiber diameters. Values in Tables A2 and A3 outside the measured range for the fiber attenuation were calculated from this model fit and are given between brackets.

The procedure to derive the camera response in the absence of a fiber is now to simply take the radiance in Tables A1–A3 and correct those for the solid angle of the lamp aperture as seen from the camera (A_{lamp}/d^2), where d is the distance between camera lens and Teflon surface of the lamp (or hole aperture in the case of the Eppley lamp). This provides the flux density at the lens of the camera.

Acknowledgments

This work was funded and managed by the Orion Thermal Protection System Advanced Development Project and the NASA Engineering and Safety Center. Mike Koop operated the ECHELLE spectrograph during the Stardust Sample Return Capsule (SRC) entry observing campaign and provided accurate timing data. Claire Webb of Vasar College, while a Research Experience for Undergraduates student at the SETI Institute, performed calibration measurements of the Ocean Optics lamps. Dave Landis of Ocean Optics advised on the LS-1-CAL calibration lamps. The LSC0207 lamp was recalibrated by Jim Niswender of Ocean Optics. David Bogdanoff of NASA Ames Research Center (ARC) operated the EPT-1379 calibration lamp. The lamp calibration plate aperture hole diameter was measured by F. Torres of the ARC Hardware Development Inspection Services (code PHX). Catalina Scientific of Tucson, Arizona, provided support during instrument assembly and characterization. Dave E. Jordan of ARC acted as the NASA Program Manager for the mission and designed methods for instrument installation. Jeff Ignaitis from M&O Precision Machining designed and built instrument-mounting hardware. Jeff Myers of the University of California, Santa Cruz, Airborne Sensor Facility at ARC measured the transmission of the DC-8 window. Calculations of expected emission levels by Mike Wright and Joe Olejniczak at ARC made it possible to set the instrument settings correctly. Jim Albers of Lockheed Martin calculated SRC viewing angles and supported the public outreach effort. Creon Levit of ARC calculated the relative distances to the approach trajectory. MODTRAN was developed by the U.S. Air Force Research Laboratory and Victoria School of Business and Technology in collaboration with Spectral Sciences, Inc. Haiping Su of the Airborne Science and Technology Laboratory at ARC performed the MODTRAN calculations of atmospheric extinction. Guidance was provided by the staff of the Stardust mission at NASA and the Jet Propulsion Laboratory with the California Institute of Technology, and especially by Don Brownlee of the University of Washington (Seattle), the Stardust Principal Investigator. NASA's DC-8 Airborne Laboratory was deployed by the University of North Dakota and National Suborbital Education and Research Center, under contract with NASA Wallops Flight Center.

References

[1] Jenniskens, P., Kontinos, D., Jordan, D., Wright, M., Olejniczak, J., Raiche, G., et al., "Preparing for the Meteoric Return of Stardust," *Proceedings of Dust in Planetary Systems*, SP-643, edited by A. Grapps, and E. Gruen, ESA, Paris, 2006.

[2] Kogaku, K. K., "UV-Nikkor 105 mm f/4.5. Nikon Instruction Manual," Nikon Corp., Tokyo, 1985.

[3] "SE 200 Echelle Spectrograph," Catalina Scientific, Tucson, AZ, 2003.

[4] "Intensified Retiga Monochrome Super High Sensitivity, Intensified IEEE 1394 FireWire," QImaging, Rept. 04-0006B-D, Surrey, BC, Canada, 2004.

[5] *SE2 200 Manual*, Catalina Scientific, Tucson, AZ, 2003.

[6] *DC-8 Airborne Laboratory Experimenter Hand Book*, NASA Dryden Flight Research Center, Edwards AFB, CA, 2002; http://www.espo.nasa.gov/docs/intex-na/DC8_Handbook-1.pdf [retrieved 23 Dec. 2005].

[7] Hook, R. N., and Lucy, L. B., "Image Restorations of High Photometric Quality. II. Examples," *The Restoration of HST Images and Spectra-II*, edited by R. J. Hanisch, and R. L. White, Space Telescope Science Inst., Baltimore, MD, 1994, p. 86.

[8] Lucy, L. B., "Image Restorations of High Photometric Quality," *The Restoration of HST Images and Spectra-II*, edited by R. J. Hanisch, and R. L. White, Space Telescope Science Inst., Baltimore, MD, 1994, p. 79.

[9] Kurucz, R. L., and Bell, B., "1995 Atomic Line Data," *Kurucz CD-ROM No. 23*. Smithsonian Astrophysical Observatory, Cambridge,

MA, 1995.
[10] Winter, M., and Herdrich, G., "Spectroscopic Observation of the Stardust Re-Entry in the Near UV," AIAA Paper 2007-4050, Miami, FL, June 2007.
[11] *NIST Handbook 150-2E*, National Inst. of Standards and Technology, Gaithersburg, MD, 2001.
[12] Taylor, M. J., and Jenniskens, P., "Near-IR Spectroscopy of Stardust Sample Return Capsule Entry: Carbon Detection," *Journal of Spacecraft and Rockets* (to be published).
[13] McHarg, M. G., Stenbeak-Nielsen, H. C., Kanmae, T., and Jenniskens, P., "Observations of the Stardust Sample Return Capsule Using a High Frame Rate Slit-Less Spectrograph," *Journal of Spacecraft and Rockets* (submitted for publication).
[14] Anderson, G. P., Berk, A., Acharya, P. K., Matthew, M. W., Bernstein, L. S., Chetwynd, J. H., et al. "MODTRAN4: Radiative Transfer Modeling for Remote Sensing," *Algorithms for Multispectral, Hyperspectral, and Ultraspectral Imagery VI*, edited by S. S. Chen, M. R. Descour, Proceedings of SPIE: The International Society for Optical Engineering, Vol. 4049, SPIE, Bellingham, WA, 2000, pp. 176–183.
[15] Jenniskens, P., and Wercinski, P. F., "Digital Still Snapshots of the Stardust Sample Return Capsule Entry," *Journal of Spacecraft and Rockets* (to be published).
[16] Kiedron, P. W., Michalsky, J. J., Berndt, J. L., and Harrison, L. C., "Comparison of Spectral Irradiance Standards Used to Calibrate Shortwave Radiometers and Spectroradiometers," *Applied Optics*, Vol. 38, No. 12, 1999, pp. 2432–2439. doi:10.1364/AO.38.002432
[17] Trumble, K. A., Cozmuta, I., Sepka, S., Jenniskens, P., and Winter, M., "Post-Flight Aerothermal Analysis of the Stardust Sample Return Capsule," *Journal of Spacecraft and Rockets*, Vol. 47, No. 5, 2010, pp. 765–774. doi:10.2514/1.41514
[18] Palmer, J. M., and Grant, B. G., *The Art of Radiometry*, SPIE Press, Bellingham, WA, 2009, p. 393.
[19] Palmer, J. M., *Radiometry and Photometry FAQ*, Optical Sciences Center, Univ. of Arizona, Tucson, AZ, 2003, p. 14.

D. Kontinos
Guest Editor